ARTICLE IN PRESS

Remote Sensing of Environment xxx (xxxx) xxx–xxx

Contents lists available at ScienceDirect

Remote Sensing of Environment

journal homepage: www.elsevier.com/locate/rse

Geomorphometric analysis of the 2014–2015 Bárðarbunga volcanic eruption, Iceland

Mariel Dirscherl[a,b,*], Cristian Rossi[a,c]

[a] Remote Sensing Technology Institute, German Aerospace Center (DLR), D-82234 Oberpfaffenhofen, Germany
[b] Department of Geography, University College London (UCL), London WC1E 6BT, UK
[c] Satellite Applications Catapult, Harwell Oxford OX11 0QR, UK

ARTICLE INFO

Keywords:
Digital elevation model (DEM)
DEM uncertainty
TanDEM-X
Volcanology
Volumetric change
Bárðarbunga
Holuhraun

ABSTRACT

Topographical information is of fundamental interest for a wide range of disciplines including glaciology, agriculture, communication network planning, or hazard management. In volcanology, elevation data are of particular importance when assessing material flows throughout a volcanic system. To obtain accurate estimates of time-varying topography in volcanic active regions, high-resolution digital elevation models (DEMs) are required. To monitor and evaluate topographical changes and especially volumetric gains and losses during the 2014–2015 Bárðarbunga eruption, Iceland, multi-temporal TanDEM-X DEM sequences were evaluated.

The 2014–2015 volcanic eruption was associated with the rare event of a caldera collapse, visible on the surface of the Vatnajökull glacier, as well as major lava effusion in the Holuhraun plain. Before investigating topographical change at the two study areas, the TanDEM-X DEMs were analysed for absolute and relative height errors resulting from the radar system parameters, the SAR processing or the local environment. The uncertainty investigation determined that acquisitions over the snow-covered Bárðarbunga caldera were primarily affected by microwave penetration into snow and DEMs over the Holuhraun lava field exhibited increased height errors due to active lava flows and dynamic outwash plain.

The topographical analysis of the 2014–2015 Bárðarbunga eruption revealed a maximum vertical displacement of approximately −65 m and +43 m at the study area of the Bárðarbunga caldera and Holuhraun lava field respectively. With a total subsidence volume of $-1.40 \pm 0.13\ km^3$ and a dense-rock equivalent (DRE) lava volume of $+1.36 \pm 0.07\ km^3$, known uncertainties in volume were decreased by approximately 35% and 77% accordingly. Taking into account the calculation of rates, the temporal development of caldera collapse and lava effusion was found to exhibit a near-exponential decrease. The ratio between subsidence and DRE lava volume moreover indicated the coupling between piston collapse and magma drainage.

1. Introduction

Iceland's neovolcanic zone is one of the most active volcanic areas in the world. Eruptions tend to occur every three to four years with a wide range of direct and indirect consequences affecting human populations and their natural environment at all spatial scales (Gudmundsson et al., 2008). The most hazardous consequences in Iceland are lava flows, lahars, pyroclastic flows, glacier outburst floods and the ejection of tephra and volcanic gas (Gudmundsson et al., 2008). Apart from the emission of volcanic gas, the hazard during the 2014–2015 volcanic eruption in the subglacial Bárðarbunga volcanic system was the large-scale effusion of lava (Gíslason et al., 2015) as well as the likelihood of a devastating glacier flood, also referred to as "Jökulhlaup" (Björnsson, 2003). Lava flows during effusive eruptions can travel over large distances and repetitively led to the destruction of settlement area, e.g., during the 1973 eruption of Heimaey, where over 300 buildings were buried (Williams and Moore, 1983). Glacier outburst floods result from the melting of overlying glacier ice due to subglacial volcanic or geothermal activity and frequently inundate the sandur plains in the south of Iceland (Björnsson, 2003; Gudmundsson et al., 2008). Jökulhlaups and lava flows are a direct threat to the inhabitants as well as livestock and vegetation in the surrounding area and illustrate the need of an adequate and near real-time monitoring of subglacial volcanic activity.

Synthetic Aperture Radar (SAR) is an active remote sensing technology operating in the microwave frequency domain. The independence of meteorological and illumination conditions facilitates the monitoring of remote volcanic areas (Bamler and Hartl, 1998). Interferometric SAR exploits the information content of two complex SAR

* Corresponding author at: Remote Sensing Technology Institute, German Aerospace Center (DLR), D-82234 Oberpfaffenhofen, Germany.
E-mail addresses: mcd4@hi.is (M. Dirscherl), cristian.rossi@sa.catapult.org.uk (C. Rossi).

http://dx.doi.org/10.1016/j.rse.2017.10.027
Received 15 February 2017; Received in revised form 3 October 2017; Accepted 14 October 2017
0034-4257/ © 2017 The Authors. Published by Elsevier Inc. This is an open access article under the CC BY-NC-ND license (http://creativecommons.org/licenses/BY-NC-ND/4.0/).

images and can be applied to deduce topography, thus digital elevation models (DEMs) (Bamler and Hartl, 1998). For the purpose of generating a global DEM of unprecedented vertical accuracy, the German TanDEM-X mission has been established as an extension of the TerraSAR-X mission. The two satellites of the TanDEM-X mission fly in close formation ("HELIX") and enable data collections in monostatic, bistatic, or alternating bistatic interferometric modes. Due to the simultaneous data collection in the bistatic interferometric mode, temporal decorrelation and atmospheric propagation effects are mostly overcome and DEMs of high accuracy can be generated (Krieger et al., 2007). With a repeat-pass interval of 11 days, the satellite mission permits the generation of DEM time series, being especially useful to recover the temporal development of topographical variations e.g. at the location of active volcanoes (Stevens et al., 1999). A number of past studies successfully used TanDEM-X data to investigate temporal elevation changes, e.g., at glaciers (Rott et al., 2014), at agricultural fields (Rossi and Erten, 2015; Erten et al., 2016) or at active volcanoes (Albino et al., 2015; Kubanek et al., 2015; Poland, 2014). In this study, TanDEM-X DEM time series are investigated to reveal relative changes in topography during the 2014–2015 eruption of the Bárðarbunga volcano.

The Bárðarbunga volcanic system consists of an ice-covered volcano in the northwestern corner of the Vatnajökull ice cap and a fissure swarm stretching over 55 km to the northeast and 115 km to the southwest (Sigmundsson et al., 2015). The 2014–2015 volcanic unrest started on 16 August 2014 and was preceded by an intense seismic swarm and lateral dyke growth in direction of the Holuhraun plain. On 29 August 2014, an initial fissure opened up approximately 10 km north of Vatnajökull and erupted basaltic lava for a period of 4 h (Sigmundsson et al., 2015). Two days later, the activity turned into a major effusive eruption that lasted until 27 February 2015. Due to the deflation of the underlying magma chamber, the eruption was associated with the slow collapse of the snow-covered Bárðarbunga caldera, located at the surface of the Vatnajökull glacier (Sigmundsson et al., 2015). Gudmundsson et al. (2016) moreover report the formation of a number of ice cauldrons south and west of the caldera. Within Iceland, the Bárðarbunga eruption is known to be the largest effusive eruption since Laki in 1783–1784. The lava volume in the Holuhraun plain was estimated at 1.6 ± 0.3 km^3 (Gíslason et al., 2015) and is yet considerably smaller than the Laki lava flow volume (14.7 km^3 ± 1 km^3) (Thordarson and Self, 1993). The volume loss at the Bárðarbunga caldera was estimated at 1.8 ± 0.2 km^3 (Gudmundsson et al., 2016).

In order to evaluate the temporal development of topographical change during the 2014–2015 Bárðarbunga eruption, the study area is subdivided into two regions of interest (ROIs). The first ROI covers the whole extent of the Bárðarbunga caldera as well as the cauldrons south and west of it while the second ROI covers the Holuhraun lava field, located in the Dyngjusandur outwash plain north of Vatnajökull (Baratoux et al., 2011). Fig. 1 illustrates the location of the ROIs as well as the footprints of available DEM tiles within the frame of a Global Multi-resolution Terrain Elevation Data 2010 (GMTED2010) topography map of Iceland.

Due to the local surface properties, the radar system parameters or the SAR processing, DEMs can be prone to severe errors (Hanssen, 2001). To guarantee the reliability of volume computations at the Bárðarbunga caldera and Holuhraun lava field, the quality of the DEMs is analysed and significant errors are accounted for. At the location of the snow-covered Bárðarbunga caldera, DEM quality can be influenced by the penetration of radar waves into snow and lead to severe misinterpretations of the measured height (Mätzler, 1987). For the ROI of the lava field, the relative movement of active lava flows between two SAR acquisitions can lead to the decorrelation of the radar signal (Bamler and Hartl, 1998). Finally, the radar system parameters and the SAR processing can result in increased height errors and bias the elevation measurement at both study locations.

The overall aim of this study is to provide a thorough temporal analysis of topographical changes during the 2014–2015 Bárðarbunga volcanic eruption using time series of TanDEM-X digital elevation models. The findings of this study shall complete the analysis in Rossi et al. (2016), who used five TanDEM-X acquisitions between 01 August 2014 and 08 November 2014 to reveal surface changes over the Bárðarbunga caldera within the initial stage of the eruption. The study presented here focuses on the data processing and the uncertainty investigation for acquisitions spanning the entire duration of the 2014–2015 Bárðarbunga eruption. Moreover, the temporal

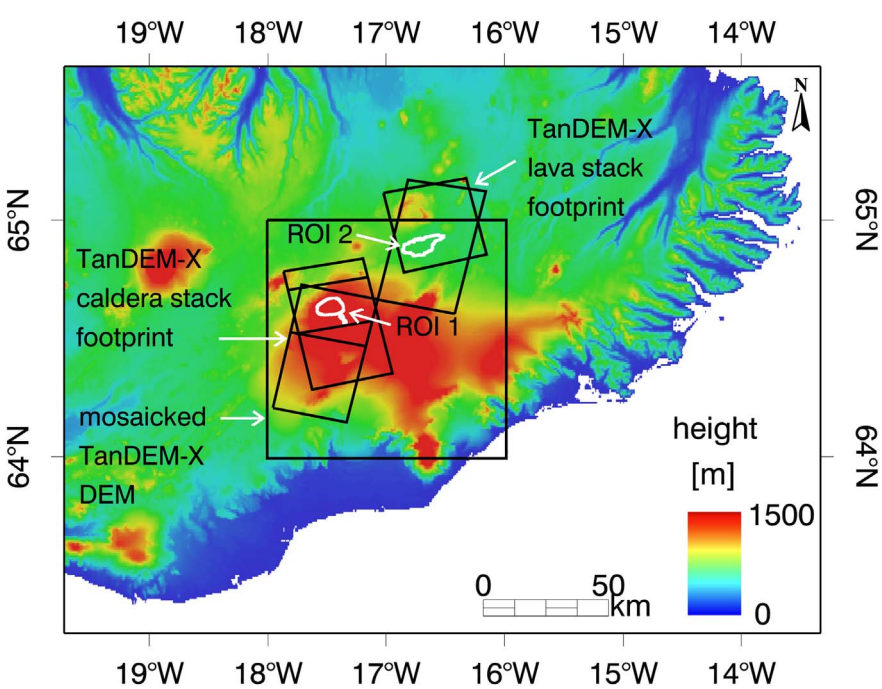

Fig. 1. Footprints of available DEM tiles over a GMTED2010 topography map of Iceland. The ROIs of the Bárðarbunga caldera and Holuhraun lava field are highlighted in white.

geomorphological changes at the Holuhraun plain are analysed. The available dataset and applied methodology of the uncertainty investigation and temporal analysis are described in Section 2. Sections 3 and 4 present and discuss the obtained results of the temporal analysis and Section 5 summarises the major findings of the analysis.

2. Methods

2.1. Dataset

Data stacks were produced for both, the Bárðarbunga caldera and the Holuhraun lava field (Fig. 1). Each data stack included multi-temporal DEM sequences spanning the entire duration of the eruption as well as reference DEMs representing the surface state before and after the volcanic event. For the study area of the Bárðarbunga caldera, a total amount of 13 pre-, co- and post-eruptive TanDEM-X raw DEMs were processed. The dataset of the Holuhraun lava field contained 9 co- and post-eruptive TanDEM-X raw DEMs as well as a pre-eruptive mosaicked TanDEM-X DEM. The DEMs were processed with the integrated TanDEM-X processor (ITP) at the German Aerospace Center (DLR). With more detail, the TanDEM-X raw DEMs were generated from monostatic and bistatic SAR data and have a typical extent of 30 km by 50 km. The mosaicked TanDEM-X DEM was produced at a dimension of 1 square degree and by mosaicking several TanDEM-X raw DEMs, acquired at different height of ambiguities and viewing geometries to maximise the overall quality of the DEM. The horizontal sampling of the processed TanDEM-X raw DEMs is approximately 10 m in northing and 7 m in easting and pixel spacing of the mosaicked TanDEM-X DEM is 12 m in both directions. More specific information about the DEM processing is given in Rossi et al. (2016). Additional height error maps (HEMs) (Section 2.2.1) served as reference for the uncertainty investigation. Table 1 lists the acquisition dates as well as radar system and processing parameters, provided within the integrated TanDEM-X processor (ITP) product file. The mean height error of the full TanDEM-X scene ($\bar{h}_{err}$) and the mean height error of the ROI ($\bar{h}_{err}^{roi}$) (sixth and seventh column in Table 1) were computed as average values in the height error maps.

To investigate topographical change due to lava flow emplacement and caldera subsidence only, the TanDEM-X raw DEMs and height error maps were clipped to vector layers created specifically for the chosen ROIs. The outer rim of the lava field was manually defined computing a vertically calibrated difference map between pre-eruptive mosaicked TanDEM-X and post-eruptive TanDEM-X raw DEM. To refine the result, an above-surface threshold, limited to an interval of]0, 100] metres, was applied to identify area of topographical change, therefore lava effusion only. The caldera outline was vectorised in agreement with the analysis in Sigmundsson et al. (2015) and of the Institute of Earth Sciences of the University of Iceland (Institute of Earth Sciences, 2014). The vector layer includes the Bárðarbunga caldera as well as eight minor ice cauldrons, six in the southeast of the caldera and two located at its western rim. Finally, the area of the ROI covering the Bárdarbunga caldera was approximately 69.2 km^2 and the ROI of the lava field 84.2 km^2. The exclusion of area outside the ROIs allowed us to eliminate topographical change due to other geomorphological processes from the quantitative computation of subsidence and eruption volumes and rates.

2.2. DEM uncertainty investigation

To reliably quantify topographical change during the 2014–2015 Bárðarbunga eruption, the quality of the available DEMs was analysed with respect to important factors affecting DEM quality. Significant errors were considered before calculating height changes. The intermediate results of this Section are presented and discussed in the following.

2.2.1. Analysis of system parameters

The radar system parameters and especially the perpendicular baseline, the height of ambiguity and the radar incidence angle can have a considerable impact on DEM quality. The TanDEM-X DEMs used within this study were analysed for the impact of radar system parameters using the height error maps as well as the information provided within the ITP product annotations (Table 1).

The height error $h_{err}(r, a)$ (Table 1) measures the amount of spatial decorrelation and is derived from the local coherence:

Table 1
System and quality parameters of the TanDEM-X dataset under study. From left to right, the columns represent the acquisition date, the perpendicular baseline $B_\perp$, the height of ambiguity h_{amb}, the centre radar incidence angle θ, the mean coherence $\bar{\gamma}$ of the full TanDEM-X scene, the mean height error $\bar{h}_{err}$ of the full TanDEM-X scene, the mean height error of the ROI $\bar{h}_{err}^{roi}$, the quality ratio q_{ratio} (Rossi et al., 2012) and the acquisition mode.

Acquisition date	$B_\perp$ [m]	h_{amb} [m]	θ [deg]	$\bar{\gamma}$	$\bar{h}_{err}$ [m]	$\bar{h}_{err}^{roi}$ [m]	q_{ratio}	Acquisition mode
Caldera								
01.08.2014	29.7	163.3	31.4	0.86	2.3	1.8	99.9	Bistatic
12.08.2014	31.1	156.2	31.4	0.80	2.8	1.8	99.9	Bistatic
14.09.2014	95.8	67.4	39.4	0.77	1.5	1.2	99.9	Bistatic
17.10.2014	50.2	96.6	31.4	0.92	0.9	0.7	99.9	Monostatic
28.10.2014	38.2	126.8	31.4	0.92	1.2	0.9	99.9	Monostatic
08.11.2014	57.8	84.2	31.4	0.91	0.9	0.7	100.0	Monostatic
06.12.2014	55.3	158.5	31.0	0.92	1.6	1.4	99.9	Monostatic
22.12.2014	314.0	15.4	31.3	0.64	0.5	0.5	99.9	Monostatic
02.01.2015	327.9	14.9	31.3	0.62	0.5	0.5	99.9	Monostatic
24.01.2015	187.9	28.1	31.3	0.75	0.6	0.6	99.9	Monostatic
04.02.2015	430.0	11.3	31.3	0.51	0.5	0.5	62.3	Monostatic
26.02.2015	360.2	13.7	31.3	0.56	0.5	0.5	88.6	Monostatic
25.05.2015	619.3	7.9	31.3	0.42	0.5	0.5	22.0	Bistatic
Lava field								
06.12.2014	148.1	42.2	37.3	0.86	0.5	0.4	99.9	Monostatic
22.12.2014	338.9	21.6	42.8	0.84	0.4	0.2	99.9	Monostatic
02.01.2015	550.0	13.2	42.8	0.82	0.2	0.1	98.5	Monostatic
13.01.2015	549.0	13.2	42.8	0.82	0.2	0.1	98.0	Monostatic
24.01.2015	235.2	32.7	42.8	0.87	0.4	0.3	99.9	Monostatic
04.02.2015	204.3	39.0	42.8	0.88	0.5	0.4	99.9	Monostatic
10.02.2015	568.4	10.6	37.3	0.75	0.2	0.1	91.5	Monostatic
26.02.2015	611.1	11.8	42.8	0.76	0.3	0.2	98.8	Monostatic
22.06.2015	576.5	10.5	37.1	0.66	0.3	0.1	87.1	Bistatic

$$h_{err}(r,a) = \sigma_{\phi}(r,a)\frac{h_{amb}}{2\pi} \tag{1}$$

where $\sigma_{\phi}(r,a)$ is the standard deviation of the interferometric phase for each sample in azimuth and range and h_{amb} is the height of ambiguity (third column in Table 1), equivalent to one phase cycle of 2π:

$$h_{amb} = \frac{\lambda R \sin\theta}{nB_{\perp}} \tag{2}$$

(λ: radar wavelength; R: range distance; θ: radar incidence angle; $B_{\perp}$: perpendicular baseline; $n = 1$: bistatic acquisitions; $n = 2$: monostatic acquisitions). The DEM standard error thus depends on the local coherence and increases with the height of ambiguity and small baselines (Ferretti et al., 2007; Krieger et al., 2007; Rizzoli et al., 2012; Rossi et al., 2016).

Since small heights of ambiguity can complicate the phase unwrapping procedure during the SAR processing and introduce errors in the order of the h_{amb} (Ferretti et al., 2007), the quality of the phase unwrapping processing step was analysed using the quality ratio. The quality ratio is a single value indicating the overall percentage of reliable pixel values in a DEM and is provided within the ITP annotations (Rossi et al., 2012). More comprehensive information about the individual system and quality parameters can be found in Bamler and Hartl (1998), Ferretti et al. (2007) or Hanssen (2001). Rossi et al. (2016) provide a detailed description of the impact of system parameters on DEM uncertainty for the specific case under study.

Table 1 shows the correlation between system and quality parameters for the TanDEM-X datasets used within the present study and reveals the overall smaller mean height errors for low heights of ambiguity (< 50 m) and large perpendicular baselines (> 100 m). At the same time, extremely large perpendicular baselines (> 200 m) lead to coherence loss. Inspecting the quality ratio in Table 1, only the 04 February 2015 and 25 May 2015 acquisitions over the Bárðarbunga caldera exhibit phase unwrapping errors. The corresponding volume estimates of the topographical analysis consequently have to be regarded critically and might not represent the actual surface change without proper corrections.

2.2.2. Influence of the local environment

In addition to radar system parameters, the local environment and more precisely snow, topography and the relative movement of objects are considerable influence factors on DEM quality (Hanssen, 2001). Since the theoretical considerations of topographical effects over the Bárðarbunga caldera are covered in Rossi et al. (2016), the following refers to the impact of snow over the Bárðarbunga caldera and to temporal decorrelation and topographical effects over the ROI of the Holuhraun lava field only.

From a microwaves perspective, the snow-covered Bárðarbunga caldera is a rather peculiar study area. Microwave acquisitions over snow and ice can indeed bias the surface elevation measurement in terms of a shift of the scattering phase centre. According to Rossi et al. (2016), the expected mean X-band height discrepancy with respect to the superficial height for the specific case under study is approximately 1.3 m in autumn months and consistently lower in summer months. In this analysis, this value was approximated by computing the mean shift between pairs of elevation models and accounted for by normalising the images (Section 2.3). A more detailed description of microwave penetration into snow is covered in Mätzler (1987), Richards (2009) and Rossi et al. (2016).

Due to the side-looking geometry of radar imaging systems, large variations in topography may introduce foreshortening, layover, or shadow effects that will increase the height error (Bamler and Hartl, 1998; Deo et al., 2015). The maps in Fig. 2 depict the correlation between height error and terrain slope for the 26 February 2015 TanDEM-X acquisition over the lava field. With relatively flat slopes (Fig. 2 (a)) and a ROI mean height error of 0.2 m (Table 1), topographical effects

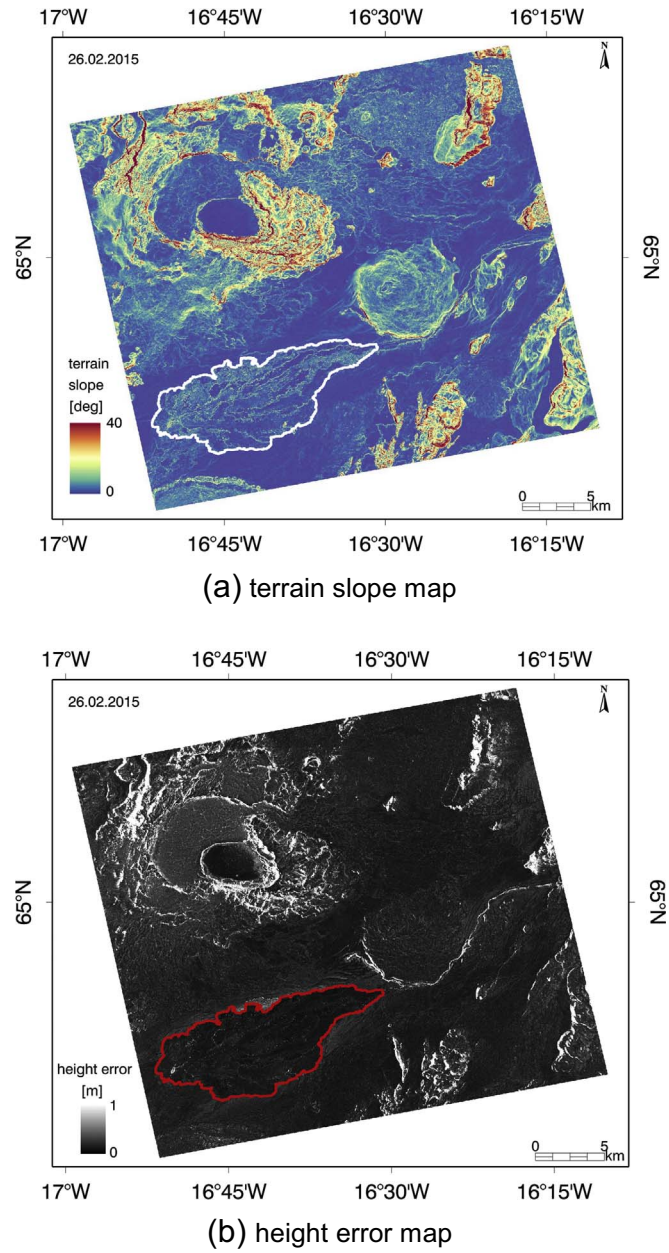

Fig. 2. Correlation between terrain slope and height errors. (a) Terrain slope computed with the 26 February 2015 acquisition. (b) Height error map of the 26 February 2015 acquisition. The extent of the lava field is outlined in white (a) and red (b). (For interpretation of the references to colour in this figure legend, the reader is referred to the web version of this article.)

were not an issue and a more detailed analysis of the individual topographical effects was not performed. The corresponding analysis over the Bárðarbunga caldera in Rossi et al. (2016) similarly revealed the absence of topographical effects over the area of interest.

Temporal terrain decorrelation arises due to the relative movement between two SAR acquisitions and can lead to the complete decorrelation of the radar signal. As shown in Table 1, the DEMs were generated from TanDEM-X data acquired in bistatic and pursuit monostatic mode. While bistatic DEMs were generated with acquisitions taken at about the same time, monostatic DEMs were produced with acquisitions with a temporal baseline of approximately 10 s. Considering the relatively slow collapse of the Bárðarbunga caldera (Sigmundsson et al., 2015), the area of the ROI was found to remain stable for both acquisition modes. Therefore, the investigation was restricted to the Holuhraun lava field, where lava erupted at the time of acquisitions

(Institute of Earth Sciences, 2014). The identification of temporally decorrelated pixels was achieved comparing height error maps to reference maps from the Institute of Earth Sciences of the University of Iceland (Institute of Earth Sciences, 2014).

Fig. 3 (a) shows the clipped height error map of the 06 December 2014 acquisition. Comparing the height errors to Landsat 8 thermal images and Sentinel-1 lava flow extent maps of the Institute of Earth Sciences of the University of Iceland (Institute of Earth Sciences, 2014), it became apparent that extremely high errors (> 10 m) mostly result from active lava flows and dynamic outwash plain within the ROI. The reference maps from the University of Iceland were acquired shortly before the acquisition date of the TanDEM-X data and confirm the applicability of height error maps to distinguish between temporally decorrelated and correlated pixels. In order to obtain a reliable volume estimate, significant errors due to temporal decorrelation had to be detected and masked from all investigated data.

2.2.3. Treatment of DEM uncertainties

The identification of unreliable height information due to temporal decorrelation can be achieved by thresholding coherence images to create binary masks (Dietterich et al., 2012; Poland, 2014). Because height errors vary according to the acquisition geometry and surface properties, the thresholds had to be adapted for each investigated acquisition.

For the 06 December 2014 acquisition shown in Fig. 3 (a), a coherence boundary value was manually chosen at 0.8. This value allowed the masking of all decorrelated areas marked in the figure. To make this process automatic, height errors larger than the sum of the mean and one standard deviation, also referred to as μ-σ-method (Laux, 2003), were flagged and manually tested.

Binary masks were generated based on the identified height error boundary values. Since the ROIs within the first two acquisitions in the data stack contained relatively large sections of lava-uncovered outwash plain, the corresponding error masks were constructed for each of the two acquisitions individually. To exclude the same proportion of pixels from data after 22 December 2014, a μ-σ-mask was generated accumulating all identified height errors for the corresponding acquisitions. The generated binary masks were

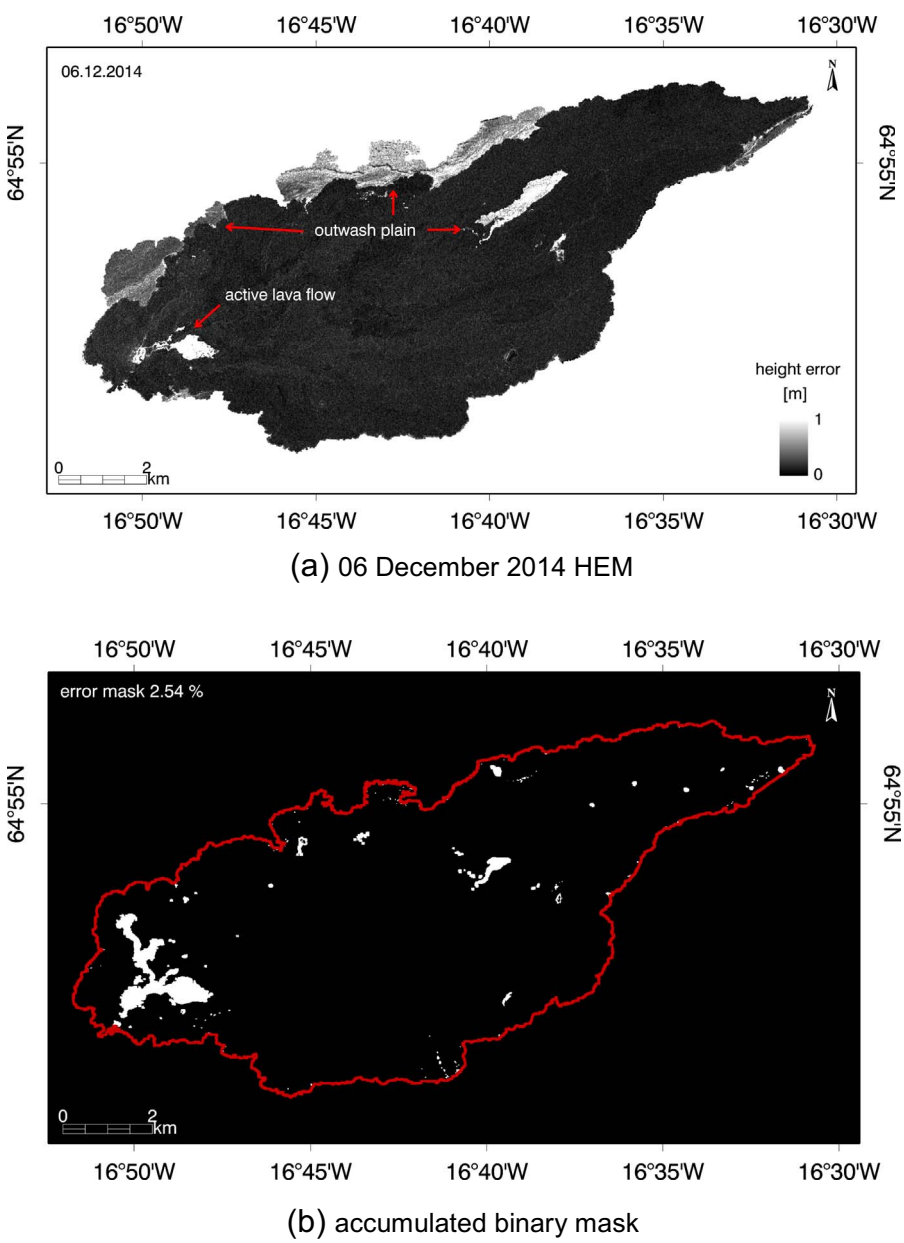

Fig. 3. (a) Height error map of the 06 December 2014 acquisition. Active lava flows and dynamic outwash plain were identified using reference maps from the Institute of Earth Sciences of the University of Iceland. (b) Accumulated binary mask applied to all DEMs and height error maps after 22 December 2014 in the lava stack. White colour represents pixels to exclude (value 0) and black colour indicates pixels to maintain (value 1). The red boarder highlights the outline of the ROI of the lava field. (For interpretation of the references to colour in this figure legend, the reader is referred to the web version of this article.)

then applied to all DEMs and height error maps relevant for the volume computation in Section 2.3.1. Fig. 3 (b) shows the accumulated mask applied to all data after 22 December 2014. The binary mask excludes an area of approximately 2.54% from the ROI and consequently led to a slight underestimation of the final lava flow volumes. Due to the low percentage of eliminated pixels, the computation of minimum lava flow volumes with binary mask was not expected to raise significantly different numbers than the estimation without mask. At the same time, volume uncertainties were expected to be considerably smaller applying a mask.

2.3. DEM temporal analysis

Variations in topography can be estimated calculating height differences between pairs of elevation models. In order to reliably quantify topographical variations between two acquisitions, detailed knowledge about the DEM errors is required (Rossi et al., 2016). Since the evaluation of absolute errors requires the availability of external references, relative changes in topography can be more easily exploited choosing a pre-eruptive acquisition as common reference (Rossi et al., 2016). The analyses in Poland (2014), Albino et al. (2015), Kubanek et al. (2015) and Rossi et al. (2016) followed this approach and revealed topographical variations in active volcanic regions. To be able to draw valid conclusions from analysing multi-temporal DEM sequences at the location of the Bárðarbunga volcano, the vertical and horizontal calibration is introduced in the following.

The calibration strategy of this analysis followed the approach proposed in Rossi et al. (2016) and absolute phase offsets were estimated with respect to a common reference DEM. In particular, the DEMs over the Bárðarbunga caldera were calibrated to the first pre-eruptive acquisition in the corresponding data stack (01 August 2014) and the DEMs covering the Holuhraun lava field were calibrated with respect to the mosaicked TanDEM-X DEM. Only small terrain portions were used for the phase calibration. Indeed, phase offsets were estimated by means of average height values over predefined, non-dynamic terrain. Comparing the mean height offsets to the average value in the corresponding reference acquisitions, the DEM vertical calibration was performed by normalising the layers, thus adding/subtracting the detected offset to/from the regarded DEM. For the area of the Bárðarbunga caldera, the determination of absolute phase offsets provided an empirical estimate of mean X-band penetration depth and the vertical calibration of the layers allowed accounting for radar penetration (Rossi et al., 2016).

The performance of the calibration was investigated evaluating cross-sections (Bárðarbunga caldera only) and pixel distributions in non-dynamic terrain in difference maps. The analysis of difference maps followed the approach in Poland (2014) and Xu and Jónsson (2014) and control areas were selected in both study regions. Considering the Gaussian distribution of pixel values, the control areas were analysed by means of a standard deviation and an average value (Poland, 2014). The average value within the pre-defined control areas is expected to be approximately 0 m for the study area of the Bárðarbunga caldera and Holuhraun lava field. Due to volumetric scattering and local variations in the seasonal snow cover, the height variances of the non-dynamic terrain portions around the Bárðarbunga caldera are expected to show slightly higher values compared to terrain portions around the lava field.

2.3.1. Volume computation

In order to show the temporal development of topographical change during the Bárðarbunga volcanic eruption, the pre-eruptive reference DEMs were subtracted from the co- and post-eruptive DEMs in the time sequences. The difference map between two DEMs then shows height changes within the acquisition interval.

The volume change ΔV was computed for each DEM pair summing the height changes within the area of the clipped ROI and multiplying it by the pixel size (70 m^2):

$$\Delta V = a \sum_i \Delta h_i \tag{3}$$

where a is the pixel area, Δh_i is the height difference of a given pixel and i is the number of pixels within the ROI (Albino et al., 2015; Poland, 2014). For the ROI of the lava field, the measured bulk lava volume was converted to its dense-rock equivalent (DRE) (or bubble-free magma) using a bulk lava density of 2600 $kg^1\ m^{-3}$ (Gíslason et al., 2015; Gudmundsson et al., 2016) and a basaltic magma density of 2750 $kg^1\ m^{-3}$ (Gudmundsson et al., 2016). The error E in the volume estimate was computed following the error propagation approach and using the height error maps (Poland, 2014):

$$E = a \sqrt{\sum_i ((h_{A_i}^{err})^2 + (h_{B_i}^{err})^2)} \tag{4}$$

where $h_{A_i}^{err}$ and $h_{B_i}^{err}$ are the pixel values of the height error maps of two DEMs. To visualise the results, difference maps were created for each DEM pair and cross-sections were analysed over selected terrain in the difference maps.

To assess the coupling between dyke intrusion and magma withdrawal during the 2014–2015 Bárðarbunga eruption, a one-to-one volume comparison was provided for completeness. For many volcanic eruptions, the volume loss deduced from surface deformation is considerably smaller than the measured volume gain in dykes and the volume ratio r_v can be in the order of 5 ± 1 (Rivalta and Segall, 2008). In this study, the volume ratio was calculated based on Rivalta and Segall (2008):

$$r_v = \frac{\Delta V_{magma}}{\Delta V_{chamber}} \tag{5}$$

(ΔV_{magma}: volume gain in dyke; $\Delta V_{chamber}$: volume loss in magma chamber).

The volume in the dyke was estimated at 0.5 ± 0.1 km^3 (Sigmundsson et al., 2015). Together with the volume loss at the Bárðarbunga caldera and the volume of DRE lava effusion, the volume ratio was approximated for acquisitions covering the same date. A more in depth description of magma compressibility can be found in Delaney and McTigue (1994), Johnson et al. (2000) or Rivalta and Segall (2008).

2.3.2. Computation of rates

The computed DRE volume was then referred to the time interval since the eruption onset. Since there still exists confusion regarding the exact definition of lava effusion or eruption rates, the parameters were calculated based on the analysis in Harris et al. (2007). In this study, eruption rates were defined as the total DRE volume at a given point in time divided by the duration since the eruption onset. The average eruption rate then represents the mean of all eruption rates. The mean output rate, on the other hand, was computed by dividing the total erupted DRE volume by the total eruption duration. Eruption rates were indicated in DRE volume per time [$m^3\ s^{-1}$] and displacement rates were additionally calculated in height per time [$cm^1\ d^{-1}$]. The computation in height per time was performed based upon the maximum and average bulk lava height differences within the ROI and was termed maximum displacement rate and mean displacement rate respectively. To achieve comparability, subsidence rates were computed in the same manner as lava rates but were termed mean subsidence rate and subsidence rate rather than mean output rate and eruption rate respectively.

The percentage of subsidence and erupted DRE volume over time was computed assuming the start of caldera collapse on 16 August 2014 (Riel et al., 2015; Sigmundsson et al., 2015) and the start of major lava effusion on 31 August 2014 (Gíslason et al., 2015). According to Gíslason et al. (2015), the end of subsidence and lava effusion was on 27 February 2015. Since DEMs were available for 26 February 2015, this acquisition was taken as the end date for the calculation of volume and time proportions.

3. Results of the DEM temporal analysis

3.1. Analysis of the DEM relative calibration

The verification of the DEM relative calibration was performed with control areas in difference maps and is presented in Table 2. For the Bárðarbunga caldera, the computed mean height differences were found to be around 0 m for all control areas under study and the maximum calculated standard deviation was detected at 3.03 m. The study area of the lava field implied similar mean height differences and a slightly lower maximum standard deviation of 0.97 m. While Figs. 4 (a) and 5 (a) show the location of

Table 2
Mean μ and standard deviation σ of selected control areas in difference maps over the Bárðarbunga caldera and Holuhraun lava field respectively.

Control area 1		Control area 2		Control area 3		Control area 4		Study area
μ [m]	σ [m]	μ [m]	σ [m]	μ [m]	σ [m]	μ [m]	σ [m]	
0.62	2.53	−0.01	1.96	−0.13	2.29	0.30	3.03	Caldera
0.39	0.71	0.68	0.75	−0.24	0.75	−0.12	0.97	Lava field

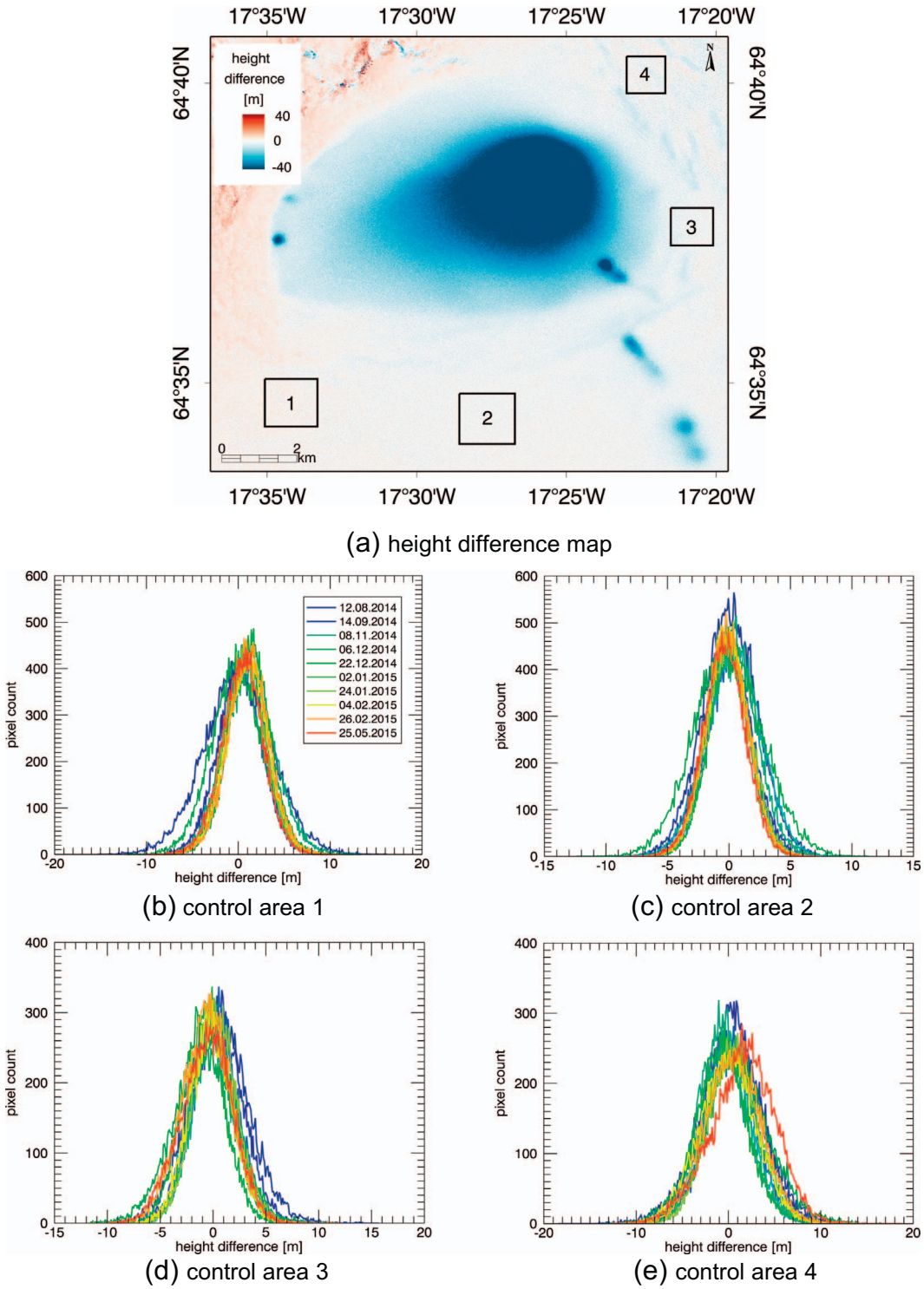

Fig. 4. (a) TanDEM-X DEM difference map between 01 August 2014 DEM and 22 December 2014 DEM. The black polygons indicate the location of selected control areas. The histograms (b–e) show the elevation distribution within the pre-defined control areas.

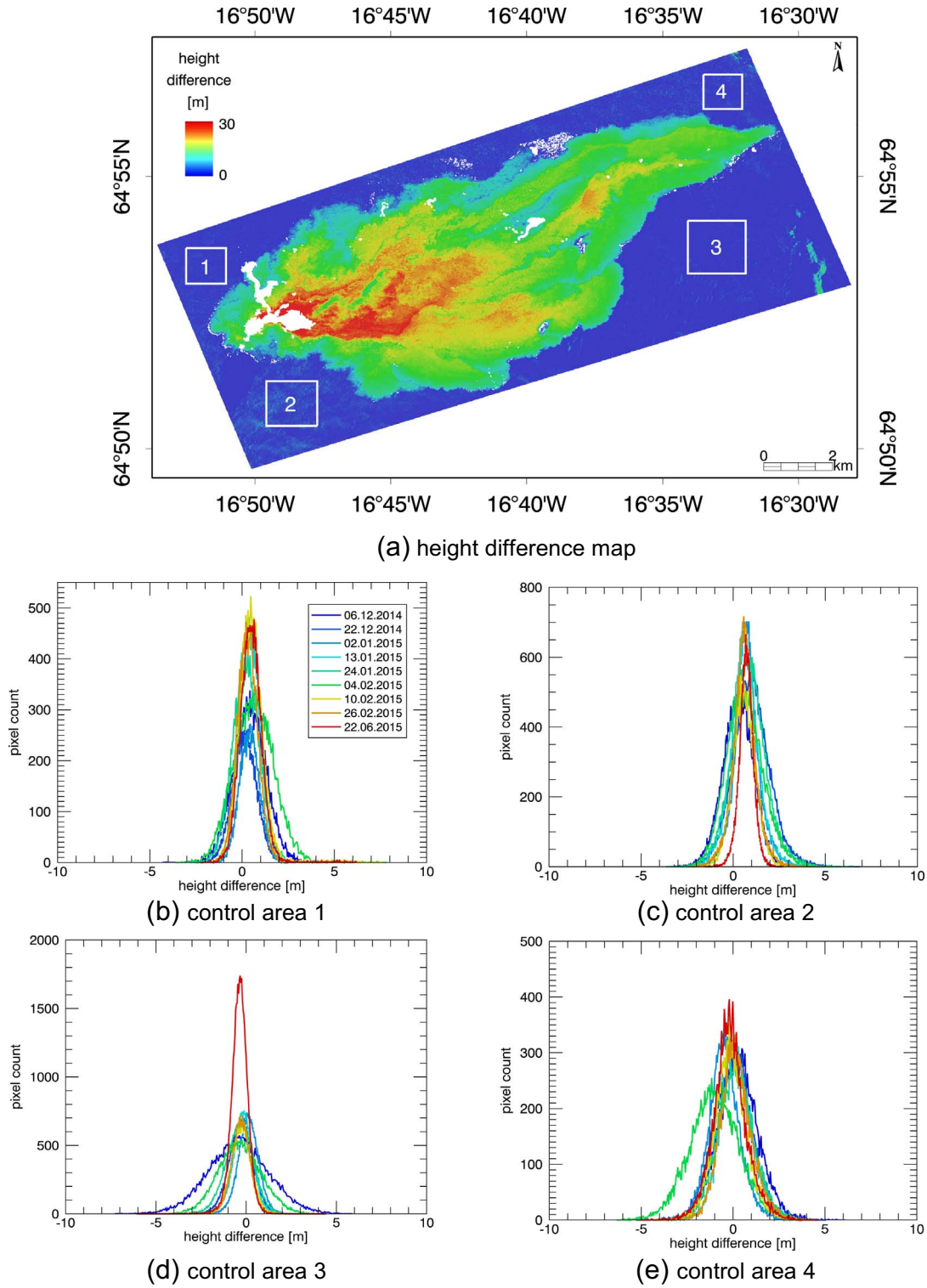

Fig. 5. (a) TanDEM-X DEM difference map between mosaicked TanDEM-X DEM and 22 December 2014 DEM. The white polygons indicate the location of selected control areas. The histograms (b–e) show the elevation distribution within the pre-defined control areas.

the selected control areas for the caldera and lava field respectively, Figs. 4 (b–e) and 5 (b–e) illustrate the pixel distributions within the control areas. The images reveal the wider spread of height values around the Bárðarbunga caldera compared to control areas around the lava field. For the control areas in Figs. 4 (b) and 5 (b–c), the distribution of pixel values shows a slight shift towards positive values (Table 2). Moreover, the 12 August 2014 (Fig. 4 (b, d)), 25 May 2015 (Fig. 4 (e)), 22 June 2015 (Fig. 5 (d)) and 04 February 2015 (Fig. 5 (e)) acquisitions deviate from the expected shape.

3.2. Topographical analysis at the location of the Bárðarbunga caldera

Fig. 6 reveals pre- and post-eruptive height changes within and around the Bárðarbunga caldera. The 12 August 2014 difference map shows only minor height fluctuations, mostly due to system noise, while the 26 February 2015 difference map clearly shows the subsided area with the major topographic change in the northeastern part of the Bárðarbunga caldera as well as in the minor cauldrons southeast and west of it.

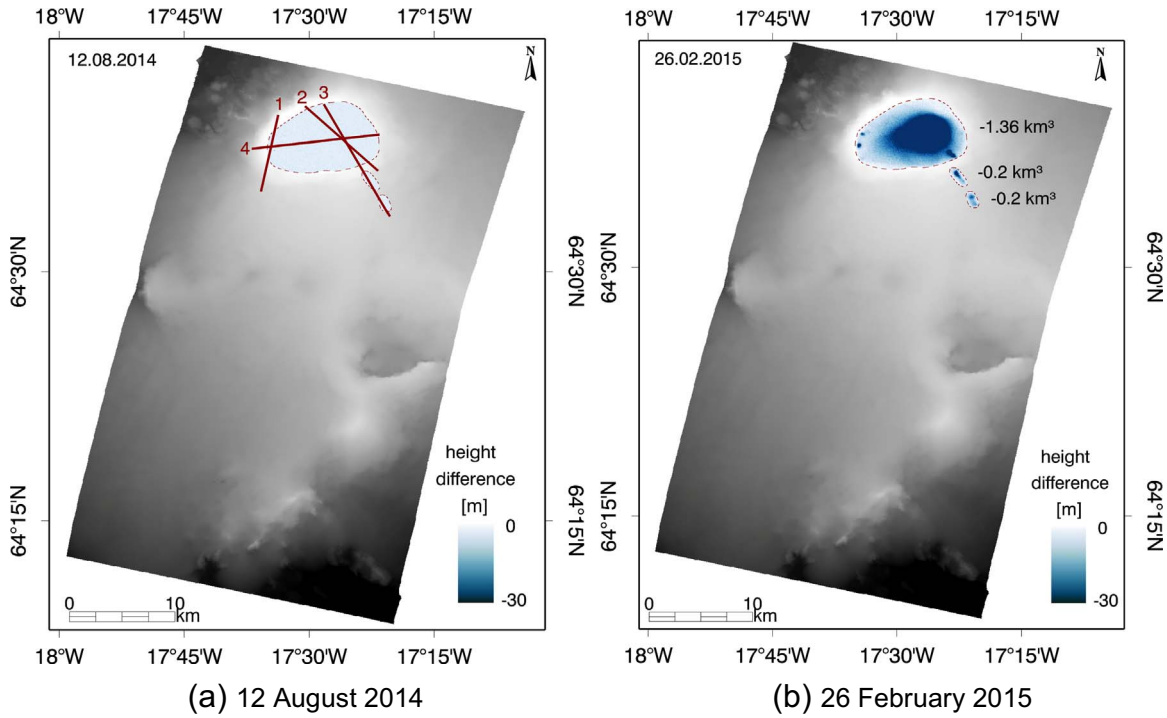

Fig. 6. TanDEM-X elevation difference maps illustrated as an overlay with the raw DEMs. (a) Difference map between 01 August 2014 DEM and 12 August 2014 DEM. The red lines illustrate the location of selected height profiles. (b) Difference map between 01 August 2014 DEM and 26 February 2016 DEM. (For interpretation of the references to colour in this figure legend, the reader is referred to the web version of this article.)

The quantitative results of the volume and rates computation are presented in Table 3. Until 26 February 2015, the subsidence volume increased and reached a final value of $-1.4 \pm 0.1\,km^3$, where $-1.36\,km^3$ subsided within the boundaries of the main caldera and $-0.02\,km^3$ within each of the minor cauldrons south of it (Fig. 6 (b)). Peak subsidence (-74.5 m) was found for 26 February 2015 and reflects the maximum height difference within the northernmost cauldron southeast of the caldera. For the area of the Bárðarbunga caldera, the maximum height difference was detected at -64.8 m. The sixth column in Table 3 lists the computed subsidence rates. With 26 February 2015 as the eruption end date, the mean subsidence rate was computed at $83.5\,m^3\,s^{-1}$. Looking at the temporal progression of all investigated rates, a decrease in subsidence over time becomes apparent. Fig. 7 shows the temporal development of maximum caldera subsidence with respect to the entire ROI.

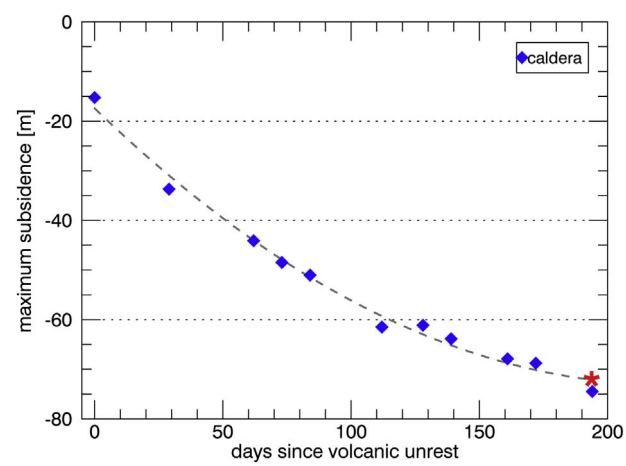

Fig. 7. Temporal development of maximum subsidence at the Bárðarbunga caldera. The red star marks the end of the eruption. (For interpretation of the references to colour in this figure legend, the reader is referred to the web version of this article.)

Table 3
Quantitative results for the ROI of the Bárðarbunga caldera. The columns represent the acquisition date, the volume change and error ΔV_{ref}, the volume proportion $V_{26.02.}$, the days since eruption onset $\Delta d_{16.08.}$, the proportion of days within the subsidence interval Δd_{active}, the subsidence rate e_s, the mean height change over the ROI $\Delta \bar{h}_{ref}^{roi}$, the mean displacement rate $\bar{d}_r$, the maximum height change within the entire ROI Δh_{max}^{roi} and the maximum displacement rate d_r^{max}.

Date	ΔV_{ref} [km^3]	$V_{26.02.}$ [%]	$\Delta d_{16.08.}$	Δd_{active} [%]	e_s [m^3 s^{-1}]	$\Delta \bar{h}_{ref}^{roi}$ [m]	$\bar{d}_r$ [cm^1 d^{-1}]	Δh_{max}^{roi} [m]	d_r^{max}[cm^1 d^{-1}]
12.08.2014	−0.02 ± 0.18	1.43 ± 12.86	–	–	–	+0.35	–	−15.25	–
14.09.2014	−0.49 ± 0.15	35.00 ± 10.71	29	14.95	195.56	−7.09	−24.45	−33.71	−116.24
17.10.2014	−0.81 ± 0.13	57.86 ± 9.29	62	31.96	151.21	−11.67	−18.82	−44.12	−71.16
28.10.2014	−0.90 ± 0.14	64.29 ± 10.00	73	37.63	142.69	−13.03	−17.85	−48.47	−66.39
08.11.2014	−0.97 ± 0.13	69.29 ± 9.29	84	43.30	133.65	−14.06	−16.74	−51.02	−60.74
06.12.2014	−1.22 ± 0.16	87.14 ± 11.43	112	57.73	126.07	−17.66	−15.77	−61.48	−54.89
22.12.2014	−1.27 ± 0.13	90.71 ± 9.29	128	65.98	114.84	−18.38	−14.36	−61.12	−47.75
02.01.2015	−1.31 ± 0.13	93.57 ± 9.29	139	71.65	109.08	−18.86	−13.57	−63.85	−45.94
24.01.2015	−1.37 ± 0.13	97.86 ± 9.29	161	82.99	98.49	−19.76	−12.27	−67.90	−42.17
04.02.2015	−1.38 ± 0.13	98.57 ± 9.29	172	88.66	92.86	−19.93	−11.59	−68.77	−39.98
26.02.2015	−1.40 ± 0.13	100.00 ± 9.29	194	100.00	83.52	−20.22	−10.42	−74.48	−38.39
25.05.2015	−1.40 ± 0.13	100.00 ± 9.29	282	145.36	–	−20.25	–	−68.74	–

The 12 August 2014 difference map in Fig. 6 shows the location of selected cross-sections and Fig. 8 illustrates the extracted height. Stretching from north to south, transect 1 (Fig. 8 (a)) covers the two minor cauldrons at the western rim of the Bárðarbunga caldera. The analysis over the difference maps reveals the depressions in the glacier surface, where the southern cauldron exhibits larger subsidence up to approximately −55 m (Fig. 8 (a)), corresponding to a local mean displacement rate of approximately 28.4 $cm^1\ d^{-1}$.

Transect 2 (Fig. 8 (b)) stretches from northwest to southeast and covers the eastern part of the Bárðarbunga caldera as well as the minor ice depressions south of it. The extracted height change reaches its maximum at the northern margin of the caldera (−58 m) and corresponds to a local mean displacement rate of approximately 29.9 $cm^1\ d^{-1}$. As visible in Fig. 8 (b), the southern ice cauldron shows its maximum height change at approximately −30 m, corresponding to a local mean displacement rate of 15.5 $cm^1\ d^{-1}$.

Cross-section 3 runs from northwest to southeast and covers the eastern part of the Bárðarbunga caldera as well as the minor ice depressions in the southeast. Fig. 8 (c) reveals the extent of subsidence with peak values around −50 m for the caldera and almost −70 m for the ice cauldrons at its southern rim. According to this, the local mean displacement rates were computed at 25.8 $cm^1\ d^{-1}$ and 36.1 $cm^1\ d^{-1}$ respectively.

The last investigated transect extends over the full width of the Bárðarbunga caldera and covers the southernmost ice cauldron at the western rim. Fig. 8 (d) reveals the shape of the caldera with the largest height change in the northeast. The maximum elevation change was measured at approximately −55 m for the Bárðarbunga caldera and ice cauldron respectively. For both depressions, this corresponds to a local mean displacement rate of 28.4 $cm^1\ d^{-1}$. Similar to all other transects, around half of the total height change within the main caldera appears to have occurred in the initial period of the eruption. The final acquisitions moreover indicate a slight height gain in areas of maximum topographic change. In non-dynamic terrain, no topographical change is visible and the acquisitions overlay each other almost perfectly.

3.3. Topographical analysis at the location of the Holuhraun lava field

The elevation difference maps in Fig. 9 reveal the temporal development of lava effusion at the location of the Holuhraun lava field. Looking at the elevation difference map between mosaicked TanDEM-X DEM and the 06 December 2014 acquisition, the ROI of the lava field was covered in most parts and the highest elevation change occurred close to the eruptive vent, located in the western part of the ROI. Until 26 February 2015, topographical change was mostly visible at the northern flanks of the flow and a major lava channel became apparent in the northeast of the ROI.

The quantitative results of the volume and rates estimation over the lava field are listed in Table 4. Until 26 February 2015, the measured bulk lava volume gradually increased and reached its final value at

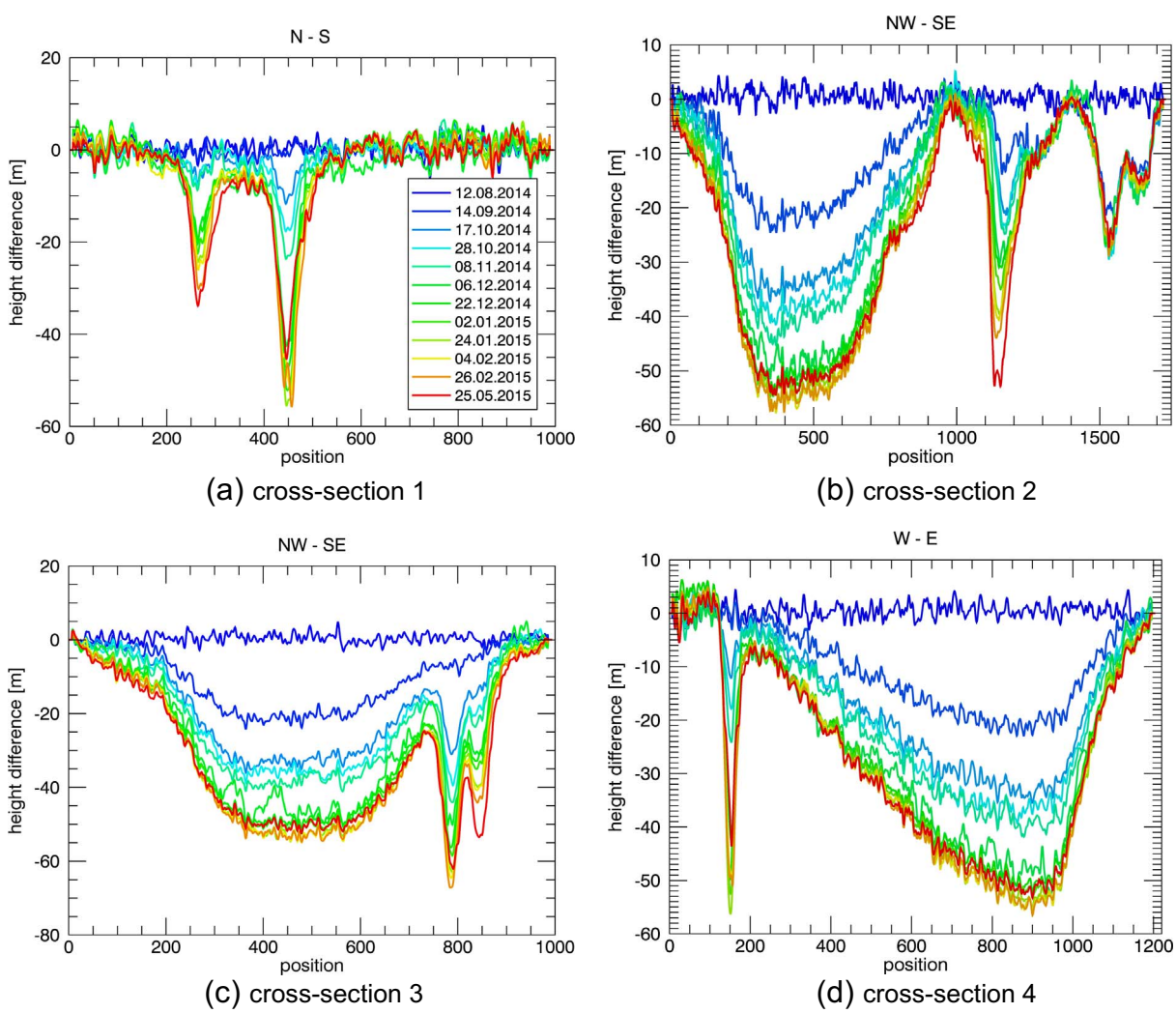

Fig. 8. Cross-sections 1 (a), 2 (b), 3 (c) and 4 (d) over the difference maps of the Bárðarbunga caldera. The location of the cross-sections is highlighted in Fig. 6 (a).

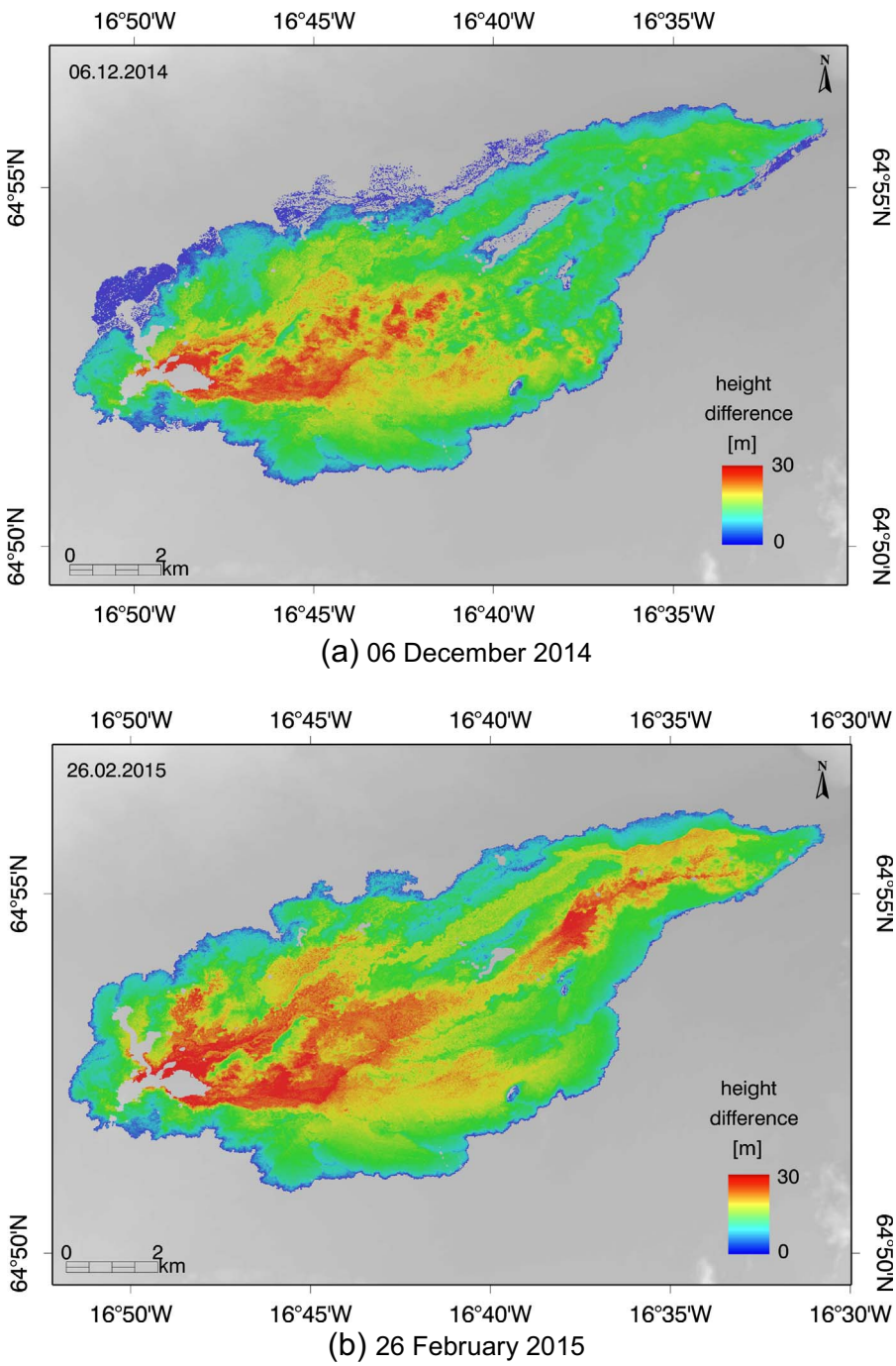

Fig. 9. TanDEM-X height difference maps illustrated as an overlay with the mosaicked TanDEM-X DEM (grey). (a) Height differences between mosaicked TanDEM-X DEM and 06 December 2014 DEM. (b) Height differences between mosaicked TanDEM-X DEM and 26 February 2015 DEM.

Table 4
Quantitative results for the Holuhraun lava field. From left to right, the columns represent the acquisition date, the bulk volume change and error ΔV_{ref}, the volume of bubble-free magma (DRE) ΔV_{DRE}, the DRE volume proportion $V_{26.02}^{DRE}$, the days since eruption onset $\Delta d_{31.08.}$, the proportion of days within the eruption interval Δd_{active}, the eruption rate e_r, the mean height change over the ROI $\Delta \bar{h}_{ref}^{roi}$, the mean displacement rate $\bar{d}_r$, the maximum height change over the ROI Δh_{max}^{roi} and the maximum displacement rate d_r^{max}.

Date	ΔV_{ref} [km^3]	ΔV_{DRE} [km^3]	$V_{26.02}^{DRE}$ [%]	$\Delta d_{31.08.}$	Δd_{active} [%]	e_r [m^3 s^{-1}]	$\Delta \bar{h}_{ref}^{roi}$ [m]	$\bar{d}_r$ [cm^1 d^{-1}]	Δh_{max}^{roi} [m]	d_r^{max} [cm^1 d^{-1}]
06.12.2014	1.19 ± 0.06	1.13 ± 0.06	83.09 ± 4.41	97	53.19	134.83	15.31	15.78	49.30	50.82
22.12.2014	1.28 ± 0.06	1.21 ± 0.06	88.97 ± 4.41	113	63.13	123.93	15.76	13.95	42.56	37.66
02.01.2015	1.34 ± 0.06	1.27 ± 0.06	93.38 ± 4.41	124	69.27	118.54	16.37	13.20	44.38	35.79
13.01.2015	1.38 ± 0.06	1.30 ± 0.06	95.59 ± 4.41	135	75.42	111.45	16.86	12.49	45.60	33.78
24.01.2015	1.41 ± 0.07	1.33 ± 0.07	97.79 ± 5.15	146	81.56	105.44	17.18	11.77	48.11	32.95
04.02.2015	1.45 ± 0.07	1.37 ± 0.07	100.74 ± 5.15	157	87.71	101.00	17.71	11.28	49.45	31.50
10.02.2015	1.43 ± 0.06	1.35 ± 0.06	99.26 ± 4.41	163	91.06	95.90	17.40	10.67	43.55	26.72
26.02.2015	1.44 ± 0.07	1.36 ± 0.07	100.00 ± 5.15	179	100.00	87.94	17.55	9.80	42.97	24.01
22.06.2015	1.42 ± 0.06	1.34 ± 0.06	98.53 ± 4.41	295	164.80	–	17.33	–	42.43	–

1.44 ± 0.07 km^3. The corresponding volume of bubble-free magma (DRE) was computed at 1.36 ± 0.07 km^3. Until 22 June 2015, the DRE lava volume decreased to 1.34 ± 0.06 km^3. Column 7, 9 and 11 list the computed rates. Assuming 26 February 2015 as the final day of the eruption, the mean output rate was computed at 87.9 m^3 s^{-1} and the average eruption rate over the whole study period was 109.9 m^3 s^{-1}.

3.4. Volume ratio and one-to-one volume and rates comparison

The computation of the volume ratio is presented in Table 5 and Fig. 10 (a–d) illustrates the quantitative results of Tables 3 and 4. With more detail, the one-to-one volume comparison in Table 5 revealed a final volume ratio of approximately 1.3, thus a slightly higher DRE and dyke (Sigmundsson et al., 2015) volume compared to caldera subsidence. Taking into account the larger subsidence as found in Gudmundsson et al. (2016), the volume ratio would approximate 1. Fig. 10 (a) shows the temporal development of lava effusion and caldera subsidence over time and Fig. 10 (b) illustrates the proportional development of the two processes. According to Fig. 10 (b), lava effusion and caldera subsidence developed similarly over time, where around 80% of the overall volume change occurred within 50% of time. In Fig. 10 (c), eruption and subsidence rates constantly decline over time and Fig. 10 (d) depicts the temporal progression of mean height changes at the Bárðarbunga caldera and Holuhraun lava field respectively. The images in Fig. 10 (a–b) reveal the overall lower error bars for volume estimates over the lava field

Table 5
Computation of the volume ratio. From left to right, the columns represent the acquisition date, the volume of bubble-free magma ΔV_{DRE}, the sum of bubble-free magma and the volume in the dyke ΔV_{magma}^{total}, the volume of caldera subsidence $\Delta V_{chamber}$ and the volume ratio r_v.

Date	ΔV_{DRE} [km^3]	ΔV_{magma}^{total} [km^3]	$\Delta V_{chamber}$ [km^3]	r_v
06.12.2014	1.13 ± 0.06	1.63 ± 0.12	−1.22 ± 0.16	1.34
22.12.2014	1.21 ± 0.06	1.72 ± 0.12	−1.27 ± 0.13	1.35
02.01.2015	1.27 ± 0.06	1.77 ± 0.12	−1.31 ± 0.13	1.35
24.01.2015	1.33 ± 0.07	1.83 ± 0.12	−1.37 ± 0.13	1.34
04.02.2015	1.37 ± 0.07	1.87 ± 0.12	−1.38 ± 0.13	1.36
26.02.2015	1.36 ± 0.07	1.86 ± 0.12	−1.40 ± 0.13	1.33

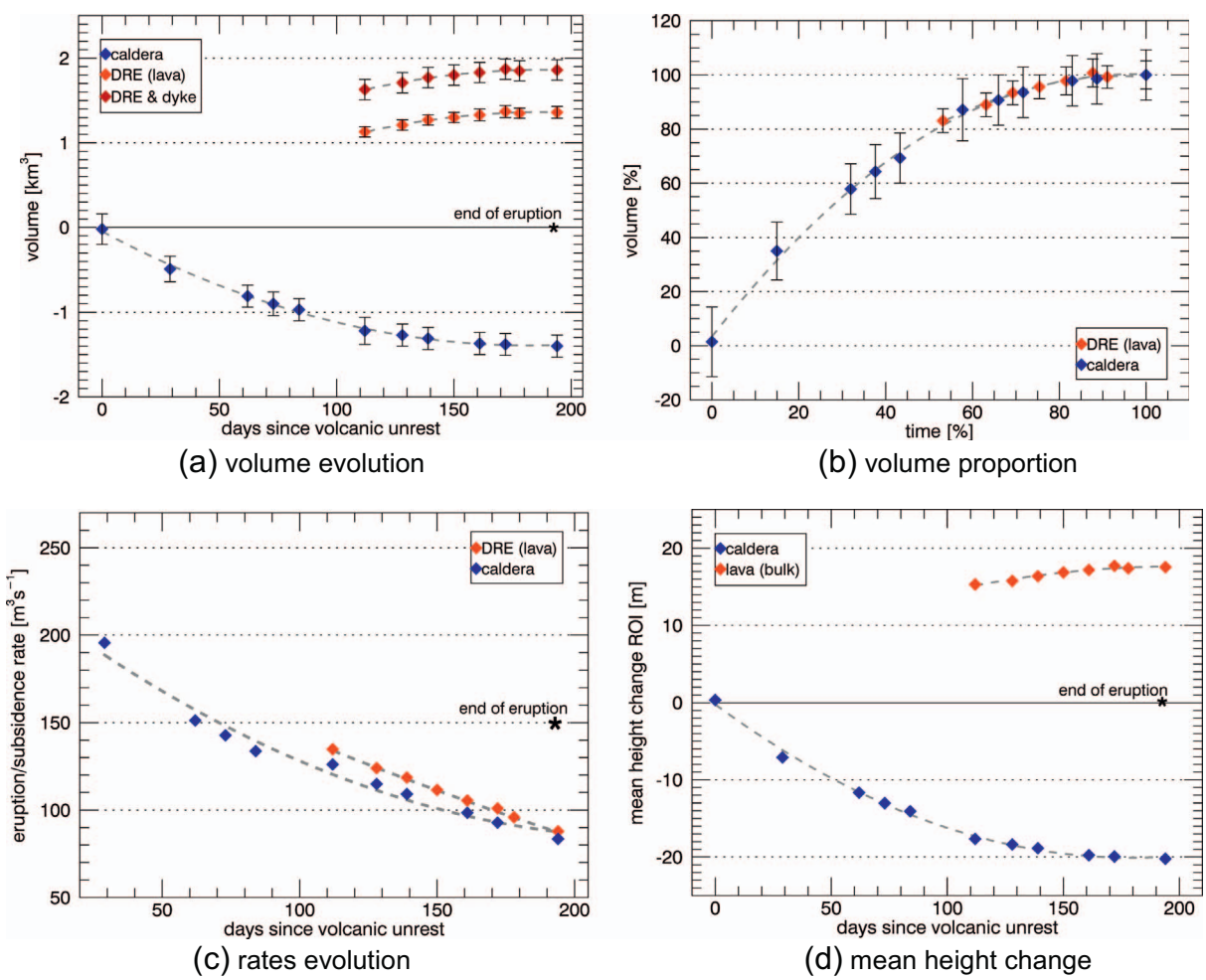

Fig. 10. Temporal development of the 2014–2015 Bárðarbunga eruption. (a) Volume evolution of magma intrusion and effusion compared to caldera subsidence. (b) Proportional development of lava effusion and caldera subsidence. (c) Temporal development of eruption and subsidence rates. (d) Evolution of mean height changes within the ROI of the Holuhraun lava field and Bárðarbunga caldera respectively.

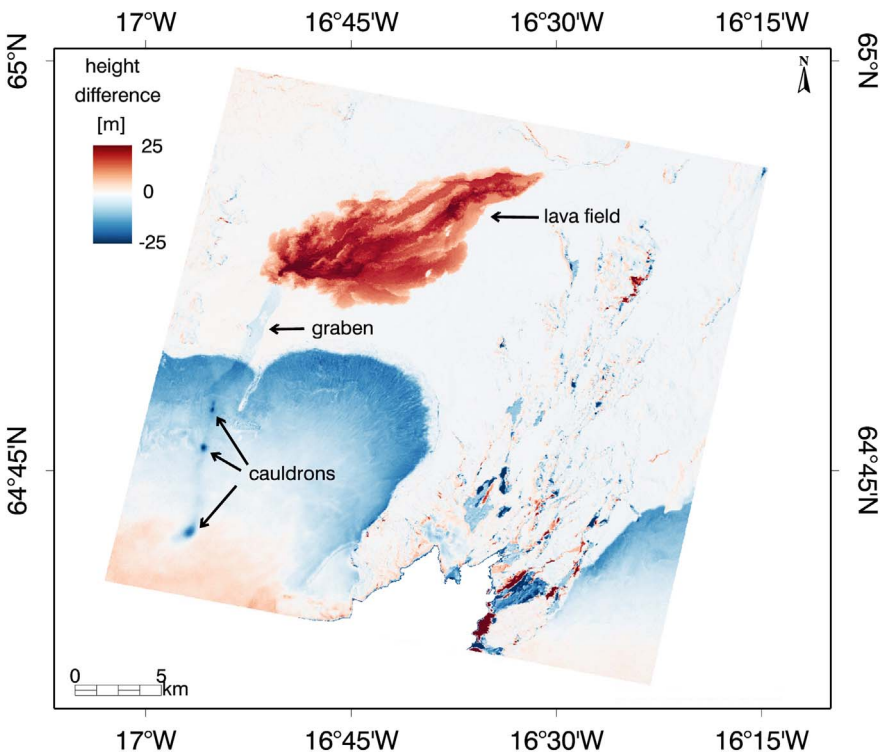

Fig. 11. Overall topographical change at the location of the Holuhraun lava field. Height changes are illustrated using a difference map between pre- (mosaicked TanDEM-X DEM) and post-eruptive DEM (22 June 2015 DEM).

compared to estimates at the location of the Bárðarbunga caldera. Fig. 11 finally shows the overall topographical change at the lava field including the propagating dyke by means of graben formation, visible on the glacier surface and in the Holuhraun plain. The graben structure is around 1 km in width and 5 m in depth.

4. Discussion

4.1. Implications of the DEM uncertainty investigation

The results in Section 2.2.1 and in Table 1 reveal the overall better quality of acquisitions over the Holuhraun lava field compared to acquisitions over the Bárðarbunga caldera. The lower quality of the dataset over the Bárðarbunga caldera is the consequence of the local surface properties and the different acquisition geometry with respect to the Holuhraun dataset. According to Table 1, large baselines over the Bárðarbunga caldera resulted in a lower mean coherence than similar baselines over the lava field, being in agreement with the analyses in Dall (2007) and Hoen and Zebker (2000), who reported a considerably lower coherence in snow-covered than in snow-free terrain. At the same time, large baselines yielded higher coherence loss than small baselines (Mätzler, 1987) (Table 1). The computation of the mean height offset between the layers raised penetration depths up to approximately 1 m in summer months and 2.6 m in winter months and supports the estimate in Rossi et al. (2016). The considerably large and varying height offsets highlight the importance of accounting for radar penetration into snow.

4.2. DEM temporal analysis of the 2014–2015 Bárðarbunga eruption

4.2.1. DEM normalisation

Moving the discussion to the temporal analysis of the Bárðarbunga eruption, the analysis of DEM normalisation in Table 2 raised the correct vertical calibration of the DEMs. The slightly increased mean height values in Fig. 4 (b) and in Fig. 5 (b–c) as well as the increased standard deviation up to 3.03 m and 0.97 m for the Bárðarbunga caldera and lava field respectively reflect the spread of height differences due to local variations in surface morphology. Minor variations in terrain height most likely occurred due to snow drift and the seasonally varying snow cover over the Vatnajökull glacier (Björnsson and Pálsson, 2008; Pálsson et al., 2014) as well as the frequent flooding of the Dyngjusandur outwash plain in the area around the lava field (Baratoux et al., 2011). The comparatively larger standard deviation over the Bárðarbunga caldera is the result of volumetric scattering. The maximum computed standard deviations are similar to the analyses in Poland (2014) and Xu and Jónsson (2014), who revealed the variances over non-dynamic, unvegetated terrain in TanDEM-X DEM difference maps at Kīlauea Volcano, Hawai'i (3.03 m), and on Jebel at Tair island in the Red Sea (1.9 m), respectively.

4.2.2. Topographical change at the Bárðarbunga caldera

DEM differencing finally revealed height and volume changes between two acquisitions. Starting with the estimates over the Bárðarbunga caldera, the visual interpretation of transects (Fig. 8) indicates the initially rapid and then slower collapse of the caldera floor. Figs. 7 and 10 (c) strengthen this assumption revealing the near-exponential decrease of peak subsidence and subsidence rates and Fig. 10 (b) shows proportional subsidence with respect to time. Gudmundsson et al. (2016) provide estimates for the temporal development of maximum caldera subsidence with 20 August 2014 as the start date and report a similar trend, confirming the obtained results in Fig. 7 with slight deviations due to the different time intervals. However, total caldera subsidence is with 1.4 ± 0.1 km^3 (26 February 2015) slightly lower than the estimation in Gudmundsson et al. (2016) (1.8 ± 0.2 km^3), probably due to a considerably smaller vector layer covering 69.2 km^2 compared to 110 km^2. The use of a smaller vector layer within the present study results from the restriction of the estimation to the main caldera, thus the vertical calibration of the DEMs to the caldera rim. Gudmundsson et al. (2016) instead estimated the area of caldera collapse analysing the subsidence of the bedrock topography with radio-echo sounding and additionally considering topographical changes up to −1 m outside the actual caldera rim. The repetitively deviating estimates as well as the increased volume error of the 06 December 2014 acquisition (Table 3) reflects undulations in the DEM.

Such noise structures can arise as a result of phase delays due to ionospheric propagation effects but are here not addressed in more detail (Massonet and Feigl, 1998; Rosen et al., 2000).

The maximum vertical displacement within the borders of the main caldera was detected at approximately −64.8 m (26 February 2015) and supports the estimate of −65 m in Gudmundsson et al. (2016). The shape and depth of transects 1 and 2 (Fig. 8 (a–b)) is in agreement with the extracted cross-sections in the corresponding TanDEM-X acquisitions and in complimentary C-band altimeter profiles in Rossi et al. (2016). Cross-section 4 and the height difference map in Fig. 4 (a), on the other hand, reflect the extracted height difference and asymmetric shape of caldera collapse in Gudmundsson et al. (2016) and in Riel et al. (2015). With the subsidence of the Bárðarbunga caldera being driven by the reactivation and slipping of pre-existing subsurface ring faults, the asymmetric collapse is most likely the result of an asymmetric geometry of the ring fault (Gudmundsson et al., 2016; Riel et al., 2015). Gudmundsson et al. (2016) used seismic data and distinct element method numerical modelling to describe the geometry of the ring-fault system as steeply outward-dipping (80°–85°) on the north side and near-vertical (85°–90°), inward-dipping on the south side. This asymmetric structure is very typical for asymmetric caldera collapses (Roche et al., 2000; Holohan et al., 2013) and has been observed, e.g., at Tendürek volcano in Turkey (Bathke et al., 2015). The larger deformation in the northeastern part of the caldera can also be seen in several one-day COSMO-SkyMed interferograms, e.g., in the 13–14 September 2014 interferogram (Riel et al., 2015) or in the 17–18 September 2014 interferogram (Gudmundsson et al., 2016; Riel et al., 2015). The slight height gain after the end of the eruption (Fig. 8 (b–d)) corresponds to winter snow accumulation and ice flow towards the centre of the caldera (Gudmundsson et al., 2016). Ice flow occurred in response to caldera collapse and led to a maximum ice thickening up to approximately 3 m (February 2015) in the region of peak subsidence (Gudmundsson et al., 2016). The observed collapse on 26 February 2015 and on 25 May 2015 includes this effect and could therefore be reduced by several metres. The minor cauldrons around the Bárðarbunga caldera as well as at the northern margin of the Vatnajökull glacier (Fig. 11) moreover indicate the occurrence of glacier floods, resulting from subglacial volcanic or geothermal activity (Björnsson, 2003). However, glacier floods were never observed and the meltwater most likely drained into the groundwater system beneath Vatnajökull (Rossi et al., 2016).

4.2.3. Topographical change at the Holuhraun lava field

DEM differencing over the Holuhraun lava field yielded a similar pattern with an extremely rapid lava effusion at the start of the eruption. Even though acquisitions were available after 06 December 2014 only, the almost complete coverage of the ROI in the earliest difference map (Fig. 9) indicates this trend. Fig. 10 again shows the near-exponential decrease of lava effusion over time. Other independent sources report the same tendency for the 2014–2015 Bárðarbunga eruption (Gudmundsson et al., 2016; Coppola et al., 2017) and Gíslason et al. (2015) report a two to three times reduced average eruption rate (100 $m^3 s^{-1}$) compared to the initial stage of the eruption. The average eruption rate of 100 $m^3 s^{-1}$ in Gíslason et al. (2015) is in good agreement with the computed average of all eruption rates in this analysis (109.9 $m^3 s^{-1}$).

According to Lipman and Banks (1987), basaltic eruptions are very commonly characterised by the reduction of lava effusion over time and Harris et al. (2000) and Wadge (1981) modelled the temporal development of fissure eruptions, e.g., at Krafla volcano, Iceland, using an exponential function of time $Q_t = Q_0 e^{-t/\tau}$, where τ is a time constant and Q_o is the initial flow rate. The considerations in Harris et al. (2000), in Lipman and Banks (1987) and in Wadge (1981) most likely explain the observed trend and were indeed modelled for the 2014–2015 Bárðarbunga eruption in Coppola et al. (2017) and in Gudmundsson et al. (2016) to confirm the agreement with the measurements of this analysis. Such modelling is particularly useful in hazard management to predict the end of volcanic eruptions.

Gíslason et al. (2015) and the Icelandic Meteorological Office (Icelandic Meteorological Office, 2015) confirm the interpretation of difference maps in Fig. 9 and similarly report the formation of rapidly growing lava channels in the northern part of the lava field as well as the almost complete coverage of the ROI in December/January with an ongoing thickening of the lava field. Considering the low error bars of the final bulk lava volume estimate (1.44 ± 0.07 km^3), the computation with masked raster layers delivered a very precise effusion volume and is similar to the approximated volumes of 1.5 ± 0.2 km^3 in Gudmundsson et al. (2016) and of 1.6 ± 0.3 km^3 in Gíslason et al. (2015). The computation with masked layers was found to be particularly important to improve the quality of the volume estimates and to eliminate unreliable height information. Comparing volume and uncertainty estimates with masked layers to computations without mask, we found that masked volume estimates were insignificantly lower while the corresponding uncertainty estimates were greatly reduced. For 06 December 2014, for instance, the bulk lava volume and uncertainty calculation with binary mask raised a volume change of 1.19 ± 0.06 km^3 and the calculation without mask raised a result of 1.23 ± 0.07 km^3. For the calculation with mask, the uncertainty and volume estimates were consequently decreased by approximately 15% and 3% respectively.

Looking at volume changes during the ongoing volcanic activity, the Institute of Earth Sciences of the University of Iceland (Institute of Earth Sciences, 2015) computed a volume of approximately 1.4 km^3 and an eruption rate of 100 $m^3 s^{-1}$ for 21 January 2015, being in good agreement with the estimated volume (1.41 ± 0.07 km^3) and eruption rate (105.44 $m^3 s^{-1}$) of the 24 January 2015 acquisition in this analysis (Table 4). With a total area of 84.2 km^2, the shape file of the lava field supports the estimate of 84.1 ± 0.6 km^2 in Gíslason et al. (2015), who used airborne SAR images to distinguish between lava flow area and outwash plain. The minor subsidence after 26 February 2015, visible in the volume computation as well as in the mean and maximum height difference estimates, can most likely be explained in terms of the cooling thus contraction of erupted lava (Lu et al., 2005; Poland, 2014; Stevens et al., 2001). Due to the masking of the raster layer, the peak height of the lava field was possibly higher than the one reported (42.97 m). However, the Icelandic Meteorological Office (Icelandic Meteorological Office, 2015) reported a maximum height of approximately 40 m on 30 December 2015, being in good agreement with the estimate on 22 December 2014 (42.56 m) (Table 4). The 06 December 2014 difference map in Fig. 9 (a) as well as computations derived from the 04 February 2015 acquisition deviated from the expected shape and show undulations in the DEM. As above, such undulations most likely occur due to ionospheric propagation effects or atmospheric perturbations caused by heat ejection from the lava field (Massonet and Feigl, 1998; Rosen et al., 2000).

4.2.4. Comparison of volume uncertainties

Comparing the estimates over the Bárðarbunga caldera to estimates over the lava field, the higher error bars for volume computations over the ROI of the caldera become apparent (Fig. 10 (a–c)). This is the result of the different surface properties and the reduction of coherence for acquisitions over snow. Furthermore, the masking of extremely high height errors for raster layers over the lava field allowed achieving a more precise uncertainty estimate with the trade-off of a slight but negligible underestimation of the total volume.

4.3. Relation between caldera subsidence and magma withdrawal

As specified in Section 2.3.1, the volume ratio can be in the order of 5 ± 1 and was calculated to assess the mechanical link between magma chamber deflation and dyke intrusion. An increased volume ratio can be explained in terms of magma sources too deep to be

recorded or more likely by the material of the host rock, the shape of the magma chamber and the magma compressibility (Rivalta and Segall, 2008; Johnson et al., 2000). The 2005 Afar dyking episode, for instance, involved a volume ratio between approximately 2.2 (Grandin et al., 2009) and 5 (Wright et al., 2006) and the volume ratio of the 1984 Krafla rifting event was estimated between approximately 5 and 6 (Árnadóttir et al., 1998). The volume ratio is equal to 1 only, when the magma is incompressible or when the bedrock material is compliable (Rivalta and Segall, 2008). For volcanic events associated with piston-like caldera collapses, volume ratios close to 1 are equally anticipated and reflect the mechanical interplay between magma withdrawal and piston collapse. With more detail, magma exiting the magma reservoir leads to a pressure drop within the chamber and causes piston failure and caldera subsidence (Geshi et al., 2002; Gudmundsson et al., 2016; Staudacher et al., 2009). The collapsing piston in turn increases the chamber pressure and almost constant pressure conditions are maintained within the magma reservoir. Consequently, the density of the magma remains stable and mass is conserved. At the same time, magma withdrawal is reinforced until a critical flow rate is reached (Coppola et al., 2017; Gudmundsson et al., 2016). According to Fig. 10 and Table 5, the volume ratio of the present study case was calculated at 1.3. With the 2014–2015 Bárðarbunga eruption being driven by piston collapse, the explained interplay between caldera collapse and magma drainage most likely explains the observed volume ratio and near-exponential decrease of caldera subsidence and lava effusion over time (Coppola et al., 2017; Gudmundsson et al., 2016).

Because of the rare occurrence of caldera collapses, only few events have been documented historically. The 2007 Piton de la Fournaise eruption on La Réunion Island, for instance, was associated with the collapse of the Dolomieu crater and a subsidence volume of approximately 0.1 km^3 (Michon et al., 2007; Staudacher et al., 2009; Urai et al., 2007). Together with the DRE magma volume (0.15 km^3; Di Muro et al., 2014), the volume ratio is in the order of 1.5 and not significantly different to the volume ratio of this analysis. Another comparable event is the 1991 eruption of Mount Pinatubo. With a DRE eruption volume of 3.7–5.3 km^3 and a caldera subsidence volume of 2.5 km^3, the volume ratio lies between 1.48 and 2.12 (Scott et al., 1996). The 2000 Miyakejima eruption similarly led to summit collapse and the formation of a caldera (Nishimura et al., 2001). The volume ratio of the Miyakejima study case equals to 1.95 and was calculated based upon a subsidence volume of 0.6 km^3 and the drainage of 1.17 km^3 of magma (Nakada et al., 2005; Nishimura et al., 2001). Although the calculation of the volume ratio presents a first approach towards deducing reservoir pressure conditions from topographical analyses only, it highlights the potential of DEM investigations for applications besides volumetric change studies.

5. Conclusion

The use of TanDEM-X elevation data has proven its excellent applicability in volcanological research. Differential DEM time series were found particularly useful to map geomorphological changes during the 2014–2015 Bárðarbunga eruption at remarkably high spatial and temporal resolution. The quantitative calculation of height and volume changes at both, the Bárðarbunga caldera and the Holuhraun lava field is in good agreement with the wider literature and confirms the utility of the applied workflow. The deduction of subsidence and eruption rates as well as the analysis of lava flow emplacement, morphology and areal extent highlights the potential of monitoring co- and post-eruptive surface changes with spaceborne SAR interferometry and is a valuable input e.g. for lava flow modelling or the further development of a near-real time monitoring of hazardous volcanic edifices to prevent volcanological hazards. Moreover, the high quality of volume estimates at both study areas allowed the computation of the volume ratio to assess the mechanical link between magma chamber deflation and dyke intrusion. Due to the high temporal resolution of the available dataset, the findings of this paper are the first of this extent for the 2014–2015 Bárðarbunga eruption.

To reveal potential errors due to the local surface properties, the imaging geometry and the system parameters, a DEM uncertainty investigation was provided for completeness. For the area of the Bárðarbunga caldera, the physical snow properties were identified as the main error source causing a shift of the scattering phase centre and introducing an elevation bias in the DEMs (Rossi et al., 2016). Active lava flows, instead, led to temporal decorrelation effects and increased height errors at the location of the Holuhraun lava field. These uncertainty sources have been estimated to be in the order of 0.14 km^3 on average in the glacier area and of 0.06 km^3 on average in the lava plain area, being considerably smaller than the lava volume uncertainty reported in Gíslason et al., 2015 (0.3 km^3) and the caldera volume uncertainty of 0.2 km^2 in Gudmundsson et al., 2016. With more detail, the high accuracy of volume changes estimated within this study reduced known uncertainties in volume by approximately 30% and 80% for the area of the Bárðarbunga caldera and the Holuhraun lava field respectively. The significant reduction of volume uncertainties again emphasises the value of accurate InSAR DEM time series for large-scale topographic change studies.

Acknowledgements

Authors would like to thank the reviewers for their valuable comments and suggestions that helped to improve this paper over all aspects. Authors would also like to acknowledge M. T. Gudmundsson, F. Sigmundsson, T. Fritz and C. Minet for the discussions on the Bárðarbunga eruption and on the TanDEM-X dataset. TanDEM-X data was provided by DLR under proposal XTIGLAC6603. Support for this work was received from the European Community's Seventh Framework Programme Grant No. 308377 (Project FUTUREVOLC).

References

Albino, F., Smets, B., d'Oreye, N., Kervyn, F., 2015. High-resolution TanDEM-X DEM: an accurate method to estimate lava flow volumes at Nyamulagira Volcano (D.R. Congo). J. Geophys. Res. Solid Earth 120, 4189–4207. http://dx.doi.org/10.1002/2015JB011988.

Árnadóttir, T., Sigmundsson, F., Delaney, P.T., 1998. Sources of crustal deformation associated with the Krafla, Iceland, eruption of September 1984. Geophys. Res. Lett. 25 (7), 1043–1046.

Bamler, R., Hartl, P., 1998. Synthetic aperture radar interferometry. Inverse Prob. 14, R1–R54.

Baratoux, D., Mangold, N., Arnalds, O., Bardintzeff, J.-M., Platevoet, B., Grégoire, M., Pinet, P., 2011. Volcanic sands of Iceland – diverse origins of aeolian sand deposits revealed at Dyngjusandur and Lambahraun. Earth Surf. Process. Landf. http://dx.doi.org/10.1002/esp.2201.

Bathke, H., Nikkhoo, M., Holohan, E.P., Walter, T.R., 2015. Insights into the 3D architecture of an active caldera ring-fault at Tendürek volcano through modeling of geodetic data. Earth Planet. Sci. Lett. 422, 157–168. http://dx.doi.org/10.1016/j.epsl.2015.03.041.

Björnsson, H., 2003. Subglacial Lakes and Jökulhlaups in Iceland. Glob. Planet. Chang. 35 (3–4), 255–271. http://dx.doi.org/10.1016/S0921-8181(02)00130-3.

Björnsson, H., Pálsson, F., 2008. Icelandic glaciers. Jökull 58, 365–386.

Coppola, D., Ripepe, M., Laiolo, M., Cigolini, C., 2017. Modelling satellite-derived magma discharge to explain a caldera collapse. Geology 45 (6), 523–526. http://dx.doi.org/10.1130/G38866.1.

Dall, J., 2007. InSAR elevation bias caused by penetration into uniform volumes. IEEE Trans. Geosci. Remote Sens. 45 (7), 2319–2324. http://dx.doi.org/10.1109/TGRS.2007.896613.

Delaney, P.T., McTigue, D.F., 1994. Volume of magma accumulation or withdrawal estimated from surface uplift or subsidence, with application to the 1960 collapse of Kīlauea Volcano. Bull. Volcanol. 56, 417–424. http://dx.doi.org/10.1007/BF00302823.

Deo, R., Rossi, C., Eineder, M., Fritz, T., Rao, Y.S., 2015. Framework for fusion ofascending and descending pass TanDEM-X raw DEMs. IEEE J. Sel. Top. Appl. Earth Obs. Remote Sens. 99, 1–9. http://dx.doi.org/10.1109/JSTARS.2015.2431433.

Di Muro, A., Métrich, N., Vergani, D., Rosi, M., Armienti, P., Fougeroux, T., Deloule, E., Arienzo, I., Civetta, L., 2014. The shallow plumbing system of Piton de la Fournaise Volcano (La Réunion Island, Indian Ocean) revealed by the major 2007 caldera-forming eruption. J. Petrol. 55 (7), 1287–1315. http://dx.doi.org/10.1093/petrology/egu025.

Dietterich, H.R., Poland, M.P., Schmidt, D.A., Cashman, K.V., Sherrod, D.R., Espinosa, A.T., 2012. Tracking lava flow emplacement on the east rift zone of Kīlauea, Hawai'i,

with synthetic aperture radar coherence. Geochem. Geophys. Geosyst. 13 (5). http://dx.doi.org/10.1029/2011GC004016.

Erten, E., Lopez-Sanchez, J.M., Yuzugullu, O., Hajnsek, I., 2016. Retrieval of agricultural crop height from space: a comparison of SAR techniques. Remote Sens. Environ. 187, 130–144. http://dx.doi.org/10.1016/j.rse.2016.10.007.

Ferretti, A., Monti-Guarnieri, A., Prati, C., Rocca, F., Massonnet, D., 2007. InSAR Principles: Guidelines for SAR Interferometry Processing and Interpretation. TM-19. ESA Publications, Noordwijk.

Geshi, N., Shimano, T., Chiba, T., Nakada, S., 2002. Caldera collapse during the 2000 eruption of Miyakejima volcano, Japan. Bull. Volcanol. 64 (1), 55–68. http://dx.doi.org/10.1007/s00445-001-0184-z.

Gíslason, S.R., Stefánsdóttir, G., Pfeffer, M.A., Barsotti, S., Jóhannsson, T., Galeczka, I., Bali, E., Sigmarsson, O., Stefánsson, A., Keller, N.S., et al., 2015. Environmental pressure from the 2014–15 eruption of Bárðarbunga volcano, Iceland. Geochem. Perspect. Lett. 1, 84–93. http://dx.doi.org/10.7185/geochemlet.1509.

Grandin, R., Socquet, A., Binet, R., Klinger, Y., Jacques, E., de Chabalier, J.-B., King, G.C.P., Lasserre, C., Tait, S., Tapponnier, P., Delorme, A., Pinzuti, P., 2009. September 2005 Manda Hararo-Dabbahu rifting event, Afar (Ethiopia): constraints provided by geodetic data. J. Geophys. Res. 114, B08404. http://dx.doi.org/10.1029/2008JB005843.

Gudmundsson, M.T., Larsen, G., Höskuldsson, Á., Gylfason, Á.G., 2008. Volcanic hazards in Iceland. Jökull 58, 251–268.

Gudmundsson, M.T., Jónsdóttir, K., Hooper, A., Holohan, E.P., Hallsdórsson, S.A., Ófeigsson, B.G., Cesca, S., Vogfjörd, K.S., Sigmundsson, F., Högnadóttir, T., et al., 2016. Gradual caldera collapse at Bárdarbunga volcano, Iceland, regulated by lateral magma outflow. Science 353 (6296). http://dx.doi.org/10.1126/science.aaf8988.

Hanssen, R.F., 2001. Radar Interferometry. Data Interpretation and Error Analysis. Kluwer Academic Publishers, Dordrecht, Netherlands.

Harris, A.J.L., Murray, J.B., Aries, S.E., Davies, M.A., Flynn, L.P., Wooster, M.J., Wright, R., Rothery, D.A., 2000. Effusion rate trends at Etna and Krafla and their implications for eruptive mechanisms. J. Volcanol. Geotherm. Res. 102, 237–270. http://dx.doi.org/10.1016/S0377-0273(00)00190-6.

Harris, A.J.L., Dehn, J., Calvari, S., 2007. Lava effusion rate definition and measurement: a review. Bull. Volcanol. 70, 1–22. http://dx.doi.org/10.1007/s00445-007-0120-y.

Hoen, E.W., Zebker, H.A., 2000. Penetration depths inferred from interferometric volume decorrelation observed over the Greenland Ice Sheet. IEEE Trans. Geosci. Remote Sens. 38 (6), 2571–2583. http://dx.doi.org/10.1109/36.885204.

Holohan, E.P., Walter, T.R., Schöpfer, M.P.J., Walsh, J.J., van Wyk de Vries, B., Troll, V.R., 2013. Origins of oblique-slip faulting during caldera subsidence. J. Geophys. Res. Solid Earth 118, 1778–1794. http://dx.doi.org/10.1002/jgrb.50057.

Icelandic Meteorological Office, 2015. http://en.vedur.is/earthquakes-and-volcanism/articles/nr/3071#thickness (Last accessed: 15 January 2017, 19:30).

Institute of Earth Sciences, University of Iceland, 2014. http://earthice.hi.is/bardarbunga_2014 (Last accessed: 5 January 2017, 14:50).

Institute of Earth Sciences, University of Iceland, 2015. http://earthice.hi.is/bardarbunga_holuhraun (Last accessed: 15 January 2017, 18:30).

Johnson, D.J., Sigmundsson, F., Delaney, P.T., 2000. Comment on "Volume of magma accumulation or withdrawal estimated from surface uplift or subsidence, with application to the 1960 collpase of Kīlauea volcano" by P. T. Delaney and D. F. McTigue. Bull. Volcanol. 61, 491–493. http://dx.doi.org/10.1007/s004450050006.

Krieger, G., Moreira, A., Fiedler, H., Hajnsek, I., Werner, M., Younis, M., Zink, M., 2007. TanDEM-X: a satellite formation for high-resolution SAR interferometry. IEEE Trans. Geosci. Remote Sens. 45 (11), 3317–3341. http://dx.doi.org/10.1109/TGRS.2007.900693.

Kubanek, J., Westerhaus, M., Schenk, A., Aisyah, N., Brotopuspito, K.S., Heck, B., 2015. Volumetric change quantification of the 2010 Merapi eruption using TanDEM-X InSAR. Remote Sens. Environ. 164, 16–25. http://dx.doi.org/10.1016/j.rse.2015.02.027.

Laux, H., 2003. Entscheidungstheorie, 5th edition. Springer Science and Business Media.

Lipman, P.W., Banks, N.G., 1987. AA flow dynamics, Mauna Loa 1984. Volcanism in Hawaii, chapter 57. In: U.S. Geological Survey Professional Paper, 1350, pp. 1527–1567.

Lu, Z., Masterlark, T., Dzurisin, D., 2005. Interferometric synthetic aperture radar study of Okmok volcano, Alaska, 1992–2003: magma supply dynamics and postemplacement lava flow deformation. J. Geophys. Res. 110, B02403. http://dx.doi.org/10.1029/2004JB003148.

Massonet, D., Feigl, K.L., 1998. Radar interferometry and its application to changes in the Earth's surface. Rev. Geophys. 36 (4), 441–500. http://dx.doi.org/10.1029/97RG03139.

Mätzler, C., 1987. Applications of the interaction of microwaves with the natural snow cover. Remote Sens. Rev. 2, 259–387. http://dx.doi.org/10.1080/02757258709532086.

Michon, L., Staudacher, T., Ferazzini, V., Bachèlery, P., Marti, J., 2007. April 2007 collapse of Piton de la Fournaise: a new example of caldera formation. Geophys. Res. Lett. 34. http://dx.doi.org/10.1029/2007GL031248.

Nakada, S., Nagai, M., Kaneko, T., Nozawa, A., Suzuki-Kamata, K., 2005. Chronology and products of the 2000 eruption of Miyakejima volcano, Japan. Bull. Volcanol. 67, 205–218. http://dx.doi.org/10.1007/s00445-004-0404-4.

Nishimura, T., Ozawa, S., Murakami, M., Sagiya, T., Tada, T., Kaidzu, M., Ukawa, M., 2001. Crustal deformation caused by magma migration in the northern Izu Islands, Japan. Geophys. Res. Lett. 28 (19), 3745–3748. http://dx.doi.org/10.1029/2001GL013051.

Pálsson, F., Gunarsson, A., Aðalgeirsdóttir, G., Jónsson, Þ., Steinsþórsson, S., Pálsson, H.S., 2014. Vatnajökull: Mass Balance, Meltwater Drainage and Surface Velocity of the Glacial Year 2013–14. Institute of Earth Sciences University of Iceland and National Power Company.

Poland, M.P., 2014. Time-averaged discharge rate of subaerial lava at Kilauea Volcano, Hawai'i, measured from TanDEM-X interferometry: implications for magma supply and storage during 2011–2013. J. Geophys. Res. Solid Earth 119, 5464–5481. http://dx.doi.org/10.1002/2014JB011132.

Richards, J.A., 2009. Remote Sensing with Imaging Radar. Springer Science and Business Media.

Riel, B., Milillo, P., Simons, M., Lundgren, P., Kanamori, H., Samsonov, S., 2015. The collapse of Bárðarbunga caldera, Iceland. Geophys. J. Int. 202, 446–453. http://dx.doi.org/10.1093/gji/ggv157.

Rivalta, E., Segall, P., 2008. Magma compressibility and the missing source for some dike intrusions. Geophys. Res. Lett. 35, L04306. http://dx.doi.org/10.1029/2007GL032521.

Rizzoli, P., Bräutigam, B., Kraus, T., Martone, M., Krieger, G., 2012. Relative height error analysis of TanDEM-X elevation data. Remote Sens. Environ. 73, 30–38. http://dx.doi.org/10.1016/j.isprsjprs.2012.06.004.

Roche, O., Druitt, T.H., Merle, O., 2000. Experimental study of caldera formation. J. Geophys. Res. 105 (B1), 295–416. http://dx.doi.org/10.1029/1999JB900298.

Rosen, P.A., Hensley, S., Joughin, I.R., Li, F.K., Madsen, S.N., Rodríguez, E., Goldstein, R.M., 2000. Synthetic aperture radar interferometry. Proc. IEEE 88 (3), 333–382. http://dx.doi.org/10.1109/5.838084.

Rossi, C., Erten, E., 2015. Paddy-rice monitoring using TanDEM-X. IEEE Trans. Geosci. Remote Sens. 53 (2), 900–910. http://dx.doi.org/10.1109/TGRS.2014.2330377.

Rossi, C., Rodriguez Gonzalez, F., Fritz, T., Yague-Martinez, N., Eineder, M., 2012. TanDEM-X calibrated Raw DEM generation. ISPRS J. Photogramm. Remote Sens. 73, 12–20. http://dx.doi.org/10.1016/j.isprsjprs.2012.05.014.

Rossi, C., Minet, C., Fritz, T., Eineder, M., Bamler, R., 2016. Temporal monitoring of subglacial volcanoes with TanDEM-X – application to the 2014–2015 eruption within the Bárðarbunga volcanic system, Iceland. Remote Sens. Environ. 181, 186–197. http://dx.doi.org/10.1016/j.rse.2016.04.003.

Rott, H., Floricioiu, D., Wuite, J., Scheiblauer, S., Nagler, T., 2014. Mass changes of outlet glaciers along theNordensjköld Coast, northern Antarctic Peninsula, based on TanDEM-X satellite measurements. Geophys. Res. Lett. 41 (22), 8123–8129. http://dx.doi.org/10.1002/2014GL061613.

Scott, W.E., Hoblitt, R.P., Torres, R.C., Self, S., Martinez, M.L., Nillos, T., 1996. Pyroclastic flows of the June 15, 1991, climactic eruption of Mount Pinatubo. In: Newhall, C.G., Punongbayan, R.S. (Eds.), Fire and Mud: Eruptions and lahars of Mount Pinatubo, Philippines. University of Washington Press, Seattle, pp. 545–570.

Sigmundsson, F., Hooper, A., Hreinsdóttir, S., Vogfjörd, K.S., Ófeigsson, B.G., Heimisson, E.R., Dumont, S., Parks, M., Spaans, K., Gudmundsson, G.B., et al., 2015. Segmented lateral dyke growth in a rifting event at Bárðarbunga volcanic system, Iceland. Nature 517, 191–195. http://dx.doi.org/10.1038/nature14111.

Staudacher, T., Ferrazzini, V., Peltier, A., Kowalski, P., Boissier, P., Catherine, P., Lauret, F., Massin, F., 2009. The April 2007 eruption and the Dolomieu crater collapse, two major events at Piton de la Fournaise (La Réunion Island, Indian Ocean). J. Volcanol. Geotherm. Res. 184, 126–137. http://dx.doi.org/10.1016/j.jvolgeores.2008.11.005.

Stevens, N.F., Wadge, G., Murray, J.B., 1999. Lava flow volume and morphology from digitised contour maps: a case study at Mount Etna, Sicily. Geomorphology 28 (3–4), 251–261. http://dx.doi.org/10.1016/S0169-555X(98)00115-9.

Stevens, N.F., Wadge, G., Williams, C.A., Morley, J.G., Muller, J.P., Murray, J.B., Upton, M., 2001. Surface movements of emplaced lava flows measured by synthetic aperture radar interferometry. J. Geophys. Res. 106 (B6), 293–313. http://dx.doi.org/10.1029/2000JB900425.

Thordarson, T., Self, S., 1993. The Laki (Skaftár Fires) and Grímsvötn eruptions in 1783–1785. Bull. Volcanol. 55, 233–263. http://dx.doi.org/10.1007/BF00624353.

Urai, M., Geshi, N., Staudacher, T., 2007. Size and volume evaluation of the caldera collapse on Piton de la Fournaise volcano during the April 2007 eruption using ASTER stereo imagery. Geophys. Res. Lett. 34 (22). http://dx.doi.org/10.1029/2007GL031551.

Wadge, G., 1981. The variation of magma discharge during basaltic eruptions. J. Volcanol. Geotherm. Res. 11 (2–4), 139–168. http://dx.doi.org/10.1016/0377-0273(81)90020-2.

Williams, R.S., Moore, J.G., 1983. Man Against Volcano: The Eruption on Heimaey, Vestmannaeyjar, Iceland. U.S. Geological Survey.

Wright, T.J., Ebinger, C., Biggs, J., Ayele, A., Yirgu, G., Keir, D., Stork, A., 2006. Magma-maintained rift segmentation at continental rupture in the 2005 Afar dyking episode. Nature 442 (7100), 291–294. http://dx.doi.org/10.1038/nature04978.

Xu, W., Jónsson, S., 2014. The 2007–8 volcanic eruption on Jebel at Tair island (Red Sea) observed by satellite radar and optical images. Bull. Volcanol. 76, 795. http://dx.doi.org/10.1007/s00445-014-0795-9.